PLOS ONE

RESEARCH ARTICLE

Measurement of normal retinal vascular pulse wave attenuation using modified photoplethysmography

Anmar Abdul-Rahman[1]*, **William Morgan**[2,3], **Dao-Yi Yu**[2,3]

1 Department of Ophthalmology, Counties Manukau DHB, Auckland, New Zealand, **2** Centre for Ophthalmology and Visual Science, The University of Western Australia, Perth, Australia, **3** Lions Eye Institute, University of WA, Perth, Australia

* anmar_rahman@hotmail.com

Abstract

Pulse wave attenuation characteristics reflect compliance and resistance properties of the vessel wall as well as initial pulse generation factors. Recently, it has become possible to measure and map the retinal vessel wall pulse wave amplitudes. Predictable pulse wave amplitude distribution may allow inferences to be made concerning vascular compliance and resistance. Twenty-eight eyes from sixteen subjects (8 male and 8 female) were examined using modified retinal photoplethysmography with simultaneous ophthalmodynamometry. This allowed the assessment of vessel wall pulsation amplitudes under a dynamic range of intraocular pressures. Pulse amplitudes were calculated using harmonic regression analysis. The pulse wave attenuation was measured under different ranges of ophthalmodynamometric force (ODF) as a function of distance along the vessel (V_{Dist}), which in turn was calculated in disc diameters (DD) from the center of the optic disc. A linear mixed-effects model with randomized slopes and intercepts was used to estimate the correlations between the logarithmically transformed harmonic regression wave amplitude (HRW_a) and the Fourier trigonometric coefficients with the predictors (V_{Dist} and ODF). The retinal venous harmonic regression wave attenuation (coefficient value±standard error) -0.40±0.065/DD, (p-value < 0.00001, 95% confidence interval (CI) -0.53 to -0.27), which was approximately twice that of the arterial -0.17±0.048/DD, (p-value < 0.0004, 95% CI = -0.27 to -0.08). There was a positive correlation between attenuation of the harmonic regression wave and ophthalmodynamometric force in both vascular systems. The attenuation of all but the sine coefficient of the second Fourier harmonic (b_{n2}) achieved statistical significance in the correlation with V_{Dist}. The cosine coefficient of the first Fourier harmonic a_{n1} was the only coefficient to achieve statistical significance in the correlation with the predictors V_{Dist} and ODF in both vascular systems. The a_{n1} coefficient value in the correlation with V_{Dist} was -3.79±0.78 and -1.269±0.37 ($p < 0.0006$), while this coefficient value in the correlation with ODF was 0.026±0.0099 and 0.009±0.04 ($p < 0.01$) in both the retinal veins and arteries respectively. The predictable attenuation characteristics in normal subjects suggest that this technique may allow the non-invasive quantification of retinal vascular compliance and other hemodynamic parameters.

OPEN ACCESS

Citation: Abdul-Rahman A, Morgan W, Yu D-Y (2020) Measurement of normal retinal vascular pulse wave attenuation using modified photoplethysmography. PLoS ONE 15(5): e0232523. https://doi.org/10.1371/journal.pone.0232523

Editor: Andrew Anderson, The University of Melbourne, AUSTRALIA

Received: September 24, 2019

Accepted: April 16, 2020

Published: May 7, 2020

Data Availability Statement: All relevant data are within the manuscript and its Supporting Information files.

Funding: The author(s) received no specific funding for this work.

Competing interests: The authors have declared that no competing interests exist.

Introduction

The vascular pulse wave is a mechanical pressure wave propagating in the wall of the blood vessel at a velocity different to that of blood flow but physiologically coupled to flow through the radially directed transmural pressure and a shear stress force, which is oriented in a parallel direction to the blood vessel wall [1, 2]. The retinal venous pulse is a useful parameter in the management of ophthalmic and systemic disorders such as glaucoma [3–5], increased intracranial pressure [6, 7], thyroid orbitopathy [8], retinal vein occlusion [9–12] and diabetic retinopathy [13, 14]. The physiologic mechanisms of the retinal venous pulse are poorly understood; being generated by the heart and transmitted via the cerebrospinal fluid space, it propagates in the wall of the central retinal vein in a retrograde direction to blood flow, entering the eye through the optic cup, where it attenuates (decays in amplitude) rapidly [13, 15]. The arterial pulse is the result of a wave of vascular wall distention, initiated by the impact of the stroke volume ejected into a closed system [16]. Amplification of the arterial pulse wave contour at points downstream is attributable to vessel wall taper. Further modification of the pulse wave contour occurs as a consequence of pulse wave reflection from junctions and discontinuities in the arterial tree [17]. In addition, there may be a frequency-dependent attenuation of the vascular pulse wave amplitude and propagation velocity by the mural viscoelastic elements. Vascular compliance is the main factor determining pulse wave attenuation through a positively correlated relationship (i.e. the higher the compliance, the higher the pulse wave attenuation) [18–21]. Compliance varies with vessel wall viscoelasticity and tension in the wall of the blood vessel per unit length (T); expressed through Laplace's law [2, 22–25] as a product of the transmural pressure (p_{tm}) and the radius (r) of the blood vessel ($T = p_{tm} \cdot r$).

To date the Dynamic Vessel Analyzer is the only commercially available method to measure the retinal vascular pulse wave properties synchronized with the cardiac cycle, which theoretically can measure retinal vascular pulse wave attenuation [26–28]. In principle it assesses retinal vessel diameter by analyzing the brightness profile of the vessel using video sequences obtained with a conventional fundus camera. To achieve an optimum contrast for vessel visualization, a green filter is inserted into the illumination pathway of the fundus camera. It is available in two versions: the retinal vessel analyzer (RVA), which is designed for research purposes and the dynamic vessel analyzer (DVA), intended for clinical use and includes a capacity to provide flicker light stimulation as a provocative test. Its adaptive algorithm, based on variation in brightness, compensates for reflections during measurement and, additionally, the instrument can automatically compensate for artifactual movements. Images deemed to be of poor quality are automatically rejected from the analysis. As with any optical device measurement accuracy is degraded with optical opacity and in patients with limited fixation. However, the main limitations include the inability to perform measurements where vessels are in close proximity or when the vessel cross-sectional diameter is <90μm [29]. Retinal vessel diameters are reported in relative units of measurement as determined by the Gullstrand eye, which can result in scaling errors if the eye has a refractive error or its dimensions vary from that of a schematic eye. Although provocative tests are possible with the DVA, there is limited data on the reproducibility of flicker responses [30].

Chen et al. described an imaging system consisting of a standard Zeiss 30° fundus camera with monochromatic red-free photographs, synchronized with the cardiac cycle using an ECG monitor connected to the camera through a time delay switch, which was set to release the camera shutter at a chosen period within 1/8th of the cardiac cycle. The changes in retinal vascular diameter were measured manually at consecutive intervals. They concluded that both retinal arterial and venous diameters underwent a change concomitant with the events of the cardiac cycle. The arterial diameter reached a maximum in mid systole, which is just after the period of peak aortic pressure, whereas the increase in intraocular pressure during systole, lead to a reduction in the retinal venous distending pressure and consequently resulted in a passive reduction of the venous diameter [31]. Limitations of this method include the manual technique used to measure vessel diameters at the same site in different image sequences and, in addition, only a single point in each vessel was examined [31]. Kumar et al. modified this technique using an image analysis method coined "Vesselness Mapping of Retinal Image Sequence", which detected and filtered vessel boundaries enhanced by the scale-space analysis of the eigenvectors of the image Hessian matrix. This technique was used to examine a longer segment of the vessel and, consequently, several pulsatile features other than spontaneous venous pulsations were detected including serpentine movements, vessel displacement and mechanical coupling. However, identification of the pulsatile segment was required before measurement [32]. Moret et al. used near-infrared slit-lamp ophthalmoscopy (HRA-OCT Spectralis) and applied principal component analysis to evaluate the image sequence. They also reported the detection of various forms of vascular pulsation including serpentine movement of the principal arteries, spontaneous venous pulsation, pulsatile movement of the entire optic nerve head, vessel displacement and mechanical coupling. Although the near-infrared illuminating light beam precluded the need for mydriasis, the advantage of this technique was offset by a low frame rate of 9 frames/second [33]. Recently swept-source optical coherence tomography was used to measure the retinal vascular axial expansion during the cardiac cycle, by analyzing the increase of the retinal thickness caused by the reversible expansion of the vessels. Using this method, Spahr et al. reported the detection of a separate retinal arterial and venous pulse wave. They detected the time delay between the two waves and estimated the pulse wave velocity in the retinal arteries to be 620±50 mm/s [34]. This is about 1,500 times faster than that measured using the RVA [27]. However, the technique failed to measure the retinal vein pulse wave velocity [34].

Photoplethysmography (PPG) is a non-invasive optical technique used to detect blood volume changes in tissue microvascular networks. The basic form of PPG technology consists of a light source to illuminate the tissue, and a photodetector to measure the variations in the intensity of transmitted or reflected light associated with changes in perfusion in the tissue volume of interest [35]. PPG technology has been used in a wide range of commercially available medical devices including the measurement of oxygen saturation [36], blood pressure [37–39], cardiac output [40, 41], the assessment of autonomic function [42, 43] and the detection of peripheral vascular disease [44–46]. The principle of operation is described by the Beer-Lambert Law, which describes the relationship between a uniform medium containing an absorbing substance and light attenuation [36]. We modified this system to objectively measure vessel pulsation amplitude from sectors of retinal images centered on the optic disc and from optic disc surface vessels, using retinal video recordings spanning three cardiac cycles [47, 48]. Modified photo-plethysmography (mPPG) allows the estimation of the attenuation of the retinal vascular pulse wave in both the retinal arteries and veins, within one disc diameter of the optic disc. In addition to being non-invasive and low cost, it offers further advantages by continuously measuring both the arterial and venous pulsation amplitudes separately. The transparent ocular refractive media allows mapping and display of the spatial distribution of the mPPG data in two dimensions. Pulse oximetry, recorded simultaneously with the optic nerve video recording, provides the necessary audio feedback, which is then used for the extracted rasterized image frames to be timed with the cardiac cycle. Time-series analysis is then used to quantify the retinal vascular pulse wave parameters. Additionally, ophthalmodynamometry adds a dynamic aspect, by altering the retinal vascular pulse amplitude over a range of intraocular pressures [47–49]. The purpose of the study was to estimate the retinal vascular attenuation non-invasively and provide the response of the attenuation characteristics to changes with induced intraocular pressure in a group of normal subjects.

Materials and methods

Healthy adult research participants were recruited from the medical student body and relatives of patients treated at the Lions Eye Institute. Written consent was obtained from each of the participants. Study approval was obtained from the University of Western Australia Human Ethics Committee adhering to the tenets of the Declaration of Helsinki. From the 32 eyes of 16 subjects, 28 were included in the analysis as four eyes were excluded due to poor image quality. Participants were required to have clear ocular media and a normal retina and optic nerve. Exclusion of a functional retinal or optic nerve pathology was determined by Humphrey standard automated perimetry or Frequency Doubling Perimetry (Humphrey Zeiss, Dublin, Ca). Subjects were not excluded based on smoking history or systemic hypertension. All subjects rested for half an hour, they had visual field testing, then dilated after another half hour. They were neither given any caffeine nor was the blood pressure measured during this period.

Ophthalmodynamometry technique

The Meditron ophthalmodynamometer (Meditron GmbH, Poststrasse, Völklingen, Germany) consists of a three-mirror Goldmann contact lens fitted at the observer end with a ring-shaped force transducer. The force transducer consists of five parts: (1) a metallic holding grip with (2) a metallic cover on the outer surface acting to compress flexible structures in the interior part of the holding grip; (3) the flexible trabeculae composed of copper-beryllium and acting as the main pressure measuring unit; (4) a metallic structure on which the trabeculae rest and (5) the plastic ring which is in contact with the contact lens and which is usually taken to hold the Goldmann contact lens [50]. The sensor ring is connected to a liquid crystal display monitor, on which the force continuously measured by the sensor ring is displayed. A foot pedal is connected to the display monitor, which is used to communicate the ophthalmodynamometric force to the display. The examination commenced with the calibration step, the observer end of the Goldman contact lens was rested on a flat surface and the device was activated. After initialization, an audio signal indicated a successful calibration. Baseline intraocular pressure was measured, the subjects' pupils were dilated with 1% Tropicamide. The Goldmann contact lens of the ophthalmodynamometer was placed on the topically anesthetized corneal surface. Contact gel was applied to the lens to ensure optical interface continuity with the cornea. The examination was performed by applying gradual increments in pressure onto the contact lens up to a constant force at the observers' discretion; the aim is to induce visible pulsations in the central retinal vein and maintain a constant force. The force measured by the sensor ring surrounding the Goldmann contact lens was then read by pressing on the foot pedal; the displayed reading was noted by a second observer. This was the endpoint of each test run. The optic nerve head was continuously imaged bio-microscopically during the examination through a Meditron Ophthalmodynamometer. The examination was repeated between 8 and 10 times for each subject to attain a range of ODF values for each eye. Videos showing excessive motion artifact, reflection from the optical media or decentration of the optic nerve in the image sequence for less than three consecutive cardiac cycles were rejected from the analysis. The ophthalmodynamometric force (ODF), displayed as Meditron units (mu), was converted to grams of force, where 1 mu = 3.33 grams of force and induced IOP = 0.89xODF+Baseline IOP in mmHg [51].

An imaging slit-lamp (Carl Zeiss, Germany) with a digital camera (Canon 5D Mark III, Japan) was used for retinal imaging. Several sequences of at least three cardiac cycles in length

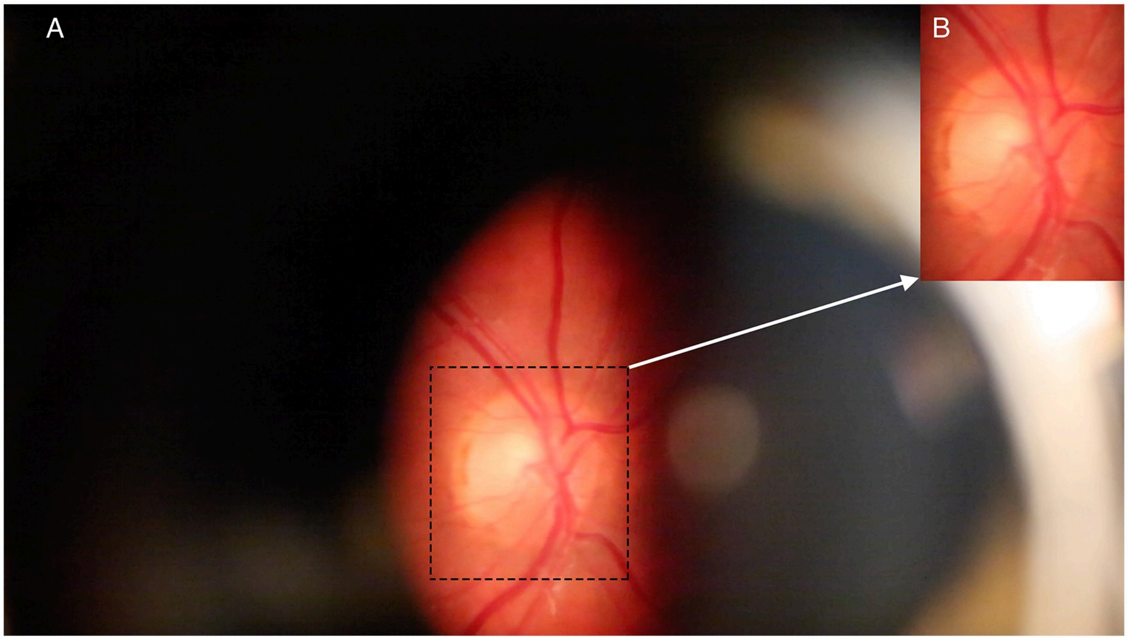

Fig 1. Example of the image zone of analysis. A) Full frame image as viewed through the Meditron ophthalmodynamometer. B) Inset showing the region of interest after cropping the image.

https://doi.org/10.1371/journal.pone.0232523.g001

were taken (each at a rate of 25 frames/second). When possible, recordings were taken from both eyes. A pulse oximeter (Nellcor N65, Covidien, Mansfield, MA) was applied to the right index finger; the audio signal from the pulse oximeter, captured with the video sequence of the optic nerve, allowed synchronization of the retinal vascular pulse with the cardiac cycle. The timing of the cardiac cycle, was generated from the audio signal from the subject's pulse oximetry recorded on the audio trace of the video segment, enabled the mathematical analysis of the periodic component from green channel transmittance. A single high quality three cardiac cycle length video recording was extracted from each raw recording session. Individual video frames were imported as separate images in (.tif) format into Photoshop (CS6). The portion of the images containing the optic disc and surrounding retina was cropped to exclude parts of the image at the boundary of the slit lamp illumination beam (Fig 1).

Principles of image analysis

All images from three cardiac cycles were analyzed in R statistical package [52]. Image analysis and segmentation are detailed in our previous work [13, 53]. The principle of the optical path length and the relationship to hemoglobin concentration is described by the Beer-Lambert Law (Eq 1).

$$A = \varepsilon(\lambda) \cdot c \cdot d = -lnT \tag{1}$$

$\varepsilon(\lambda)$ = Extinction coefficient or absorptivity of the medium for a specific wavelength (L/mmol/cm)

c = Concentration of light absorbing material which is assumed to be a constant (mmol/L)
d = Optical path length through the medium (cm)
T = Transmittance of a material sample

The isosbestic point, defined as the wavelength where light absorbance for both oxy- and deoxyhemoglobin, is approximately 550 nm (green channel), therefore the green color channel from each image layer was extracted [54, 55]. To mimic the physiology of the human eye, the Bayer filter mosaic used on video camera sensors favors the green channel due to the filter pattern arrangement of 50% green, 25% red and 25% blue, [56] The fact that there are twice as many green filters results in the green channel being the least noisy of the three color channels. There is a variation of hemoglobin content in a pulsating vessel, resulting in a fluctuating retinal light transmittance during the cardiac cycle [13]. For Eq 1 the uniform absorbance (A), is proportional to the negative logarithm of transmittance (T), this is approximated in each cardiac cycle using the green color channel and by assuming an extinction coefficient $\varepsilon(\lambda)$ of 12 L/mmol/cm at 550 nm for both oxy and deoxyhemoglobin and a hemoglobin concentration (c) of 150g/l [13]. To convert from molar extinction coefficient to absorbance a molar density of 64,500 g/mol was used and the result divided by 2 as a reflectance method assumed that light was reflected through the same vessel twice, doubling the optical path length.

$$A = \frac{\epsilon(\lambda) \cdot c \cdot d}{64,500} \cdot \frac{1}{2} \tag{2}$$

If the various assumptions are correct and absorption was limited to 550 nm then the calculated optical path length would be in microns. This value has not been validated empirically and the mathematical derivation is a marked simplification of the complexities of matching between hemoglobin transmittance, reflectance, scatter and the charge-coupled device green channel sensitivity profile. Absolute vessel dimensions would also depend upon knowledge of the incident light upon the retina to calculate absolute transmission. We substitute this information by calculating the difference in these values and their rates of change across the cardiac cycle, which also gives informative results [13].

Data processing

Image processing was done in Adobe Photoshop CS6. The video-recording was performed through an ophthalmodynamometer lens system. Individual image frames were extracted from each video sequence and saved as Tagged Image File Format (TIFF) files. Each of these images was cropped to an array of pixels with coordinates x, the pixel at location x has an associated intensity triple I(x) = (R(x), G(x), B(x)), where R, G, and B respectively describe the red, green and blue levels [57]. The intensity triples were extracted using the R package jpeg or tiff [58], with RGB values converted to the standard [0, 255] scale. Following this procedure, the data for any given video are represented as a sequence $I_1(x),I_2(x)\ldots I_M(x)$, where M is the total number of frames, typically M = 70 for each video clip to include three cardiac cycles. Each sequence of images was rasterized and aligned. Image segmentation was performed manually, by creating a set of four vessel templates to isolate portions of each image corresponding to two parts (A and B) of the lower retinal vein, the upper vein, and the artery. To account for both noise and the central vessel reflex, pixel RGB intensity appearing as almost pure white [I = (255, 255, 255)) or black (I = (0, 0, 0))], with RGB mean intensity values within 1% of either of these extremes, were excluded from the subsequent analysis. (This affected less than 0.00001% of the pixels across our video data). The mean color intensity over a template reflects the aggregate blood volume in the corresponding section of the retina; for any given template (T) the information was summarized after excluding pixels with extreme values as outlined above. The information was summarized by computing means for each of the RGB channels and plotting the time series of these values: [R(x): $x \in T$], [G(x): $x \in T$] and [B(x): $x \in T$] [47]. Data from the green channel was extracted as outlined above. A darker image was registered as having a higher intensity and therefore a thicker blood column with more hemoglobin content. Therefore, the change in the mean image intensity of the green channel, is proportional to the change in blood volume. An array of values across the entire optic disk and peripapillary retina from either 2x2 or 5x5 pixel clusters was then used to generate false-color maps based upon the values of either the amplitudes, slopes or timing information [13].

Mathematical model

A time series is any metric measured over regular time intervals [59]. In our model each data point represented by the mean of the green channel intensity (y(t)) at time (t) is measured as a fraction of the cardiac cycle, rather than in seconds. Eq 3 represents the nominal time for frame (i) in cycle (c, where c = 1-3).

$$t_i = \frac{i}{n_c} + c - 1 \tag{3}$$

where n_c = number of frames in the cth cycle.

The components of the series were expressed as a sum of the trend or regular term (f(t)) and the stationary error, irregular or residual term (ε_t) with a zero mean (Eq 4).

$$y(t) = f(t) + \epsilon_t \tag{4}$$

The trend component was decomposed into periodic $f(t)_p$ and non-periodic components $f(t)_{np}$, the latter is to account for changes in intensity due to subject movement artifact (Eq 5).

$$f(t) = f(t)_p + f(t)_{np} \tag{5}$$

The periodic trend component was modeled as a Fourier series expansion (Eq 6), this approach is used in the field of computational fluid dynamics of oscillating flow [60, 61].

$$\mathcal{F}(f(t)_p) = a_0 + \sum_{n=1}^{\infty} a_n \cdot cos(n\pi t) + b_n \cdot sin(n\pi t) \tag{6}$$

a_0 = Coefficient representing the mean of $f(t)_p$.
a_n = Coefficient of the cosine function of $f(t)_p$.
b_n = Coefficient of the sine function of $f(t)_p$.
n = Integer 0,1,2. . . etc. representing the harmonic component.

Higher harmonic frequency model comparisons were conducted using the Akaike Information Criterion (AIC). In most eyes AIC preferred models with first and second-order frequencies (Eq 6), therefore the final analysis was limited to the first and second harmonics [47].

The non-periodic component of the trend $f(t)_{np}$ was modeled using a linear spline with knots at times t = 1 and t = 2 (Eq 7). Knot frequency was based on the observation that the duration of most artifactual movements is at least one second, which in turn is approximately equal to one cardiac cycle.

$$f(t)_{np} = b_0 + b_1 t + b_2 (t-1)_+ + b_3 (t-2)_+ \tag{7}$$

where the subscript + indicates truncation below at zero, so that $z_+ = z$ for $z>0$ and $z_+ = 0$ for $z \leq 0$ [47]. The error component of the series described by Eq 3 was modeled using a first-order autoregressive process (i.e. the value of the point in the series is weighted by a value of a proceeding datapoint, separated by one lag in the time series), so as to account for residual

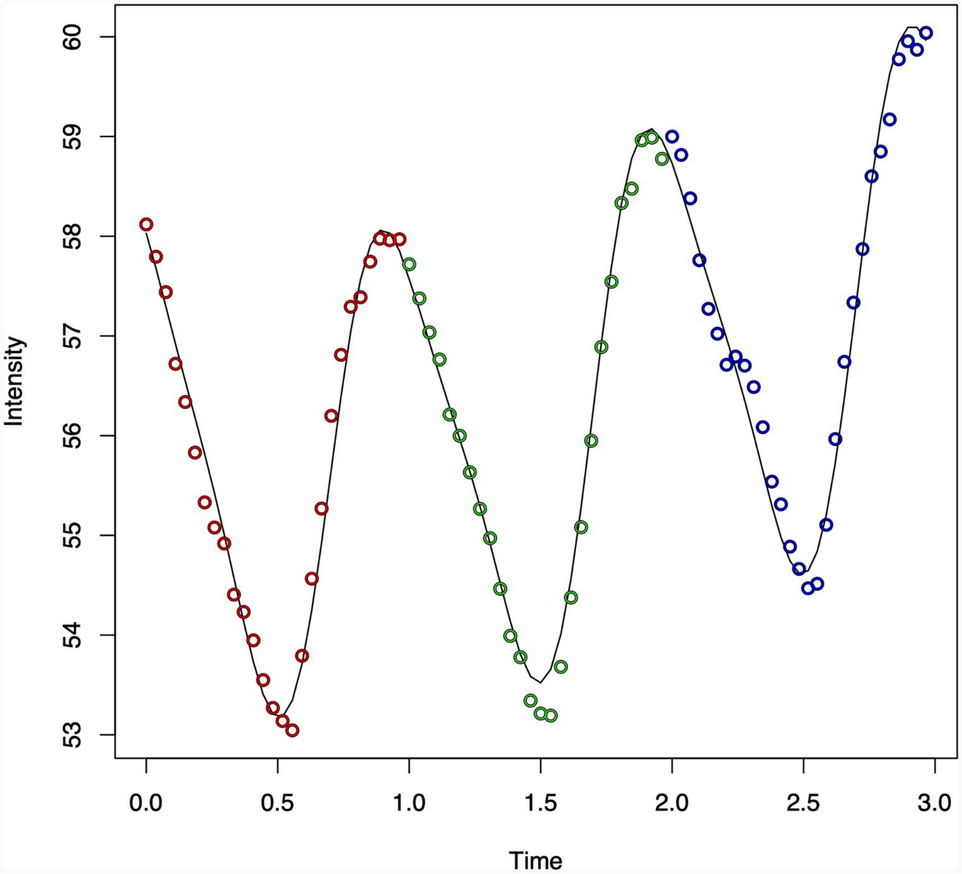

Fig 2. Harmonic regression model fit in a single case. The periodic nature of the data and harmonic regression model fit from the green channel from three cardiac cycles is demonstrated in the retinal vein from a single case. The changes in the harmonic regression waveform with changes in ODF are detailed in Figs 9 to 11.

https://doi.org/10.1371/journal.pone.0232523.g002

serial dependence in the data.

$$e_t = \rho\epsilon_{t-1} + u_t \tag{8}$$

where u_t is white noise and ρ is the autoregressive parameter estimated by restricted maximum likelihood (REML).

The periodic nature of the data and model fit from the green channel from three cardiac cycles is demonstrated for a single case in (Fig 2), the model fit for the three channels is further detailed in our earlier work [47]. A summary of the workflow is demonstrated in (Fig 3).

Statistical analysis

The harmonic regression model is a time series (Eq 3), with both a harmonic trigonometric series and autoregressive error terms. The amplitude of the composite (combined first and second harmonic waveforms) was termed the harmonic regression wave amplitude (HRW_a) [47], which was modeled for the arteries and veins separately. As the distribution of the HRW_a was non-normal, the median was used to measure central tendency; range and interquartile range

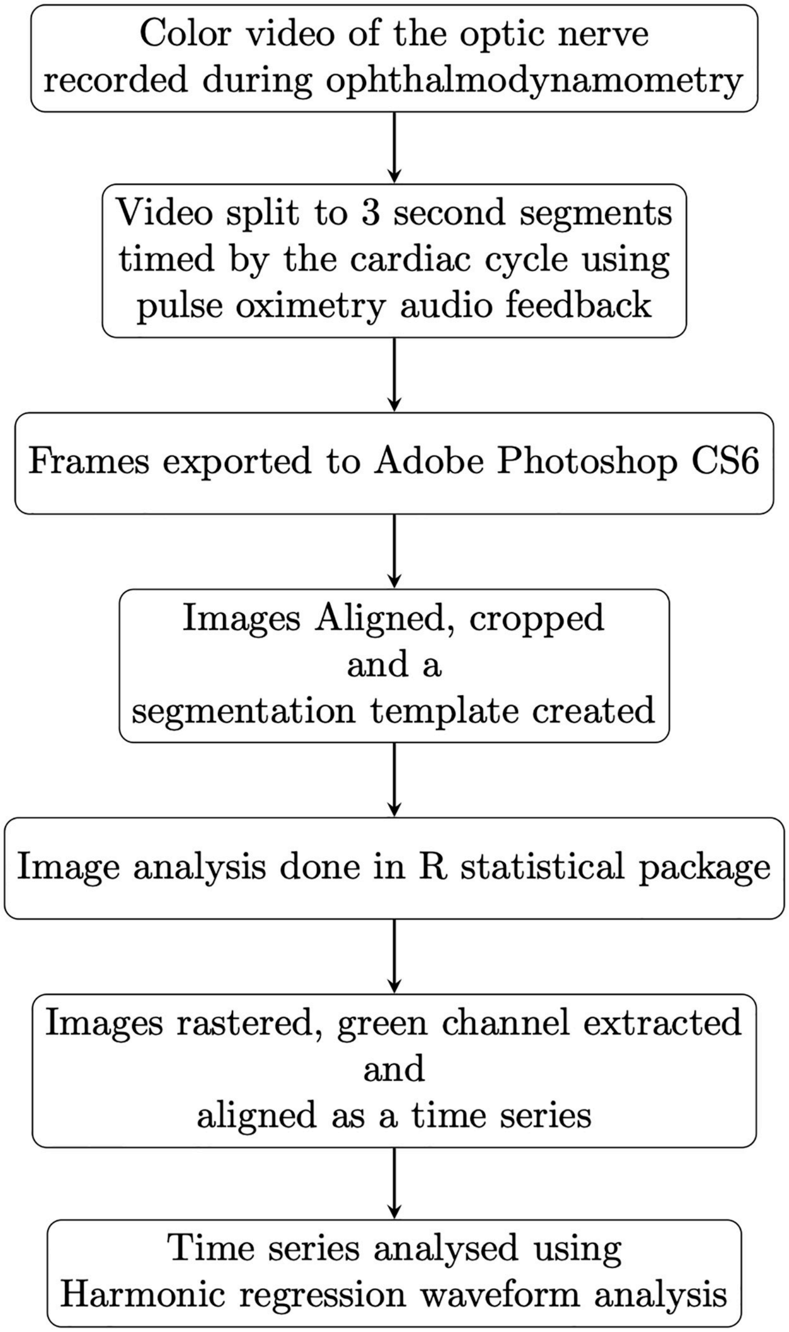

Fig 3. Summary workflow. Schematic of the technical workflow in the data acquisition and image processing.

https://doi.org/10.1371/journal.pone.0232523.g003

(IQR) were used to measure data dispersion. The Kruskal-Wallis test was used to assess the statistical significance between the median HRW_a of both vascular systems. HRW_a was normalized using logarithmic transformation, which is a recommended transformation for data skewed to the right [62]. In addition, Pearson's criteria for normality were used to confirm the appropriate transformation, these values were $HRW_{a\text{-arterial}} = 1.32$ and $HRW_{a\text{-venous}} = 3.77$, where a value closer to zero confirms the suitability of the methodology. The biological principle underpinning this transformation is the fact that viscoelastic stress-strain curves in blood vessel walls are curvilinear [19], which is approximated with a logarithmic function within the physiologic range. Analysis of variance (ANOVA) was used to estimate the F-statistic and p-value of the HRW_a for the difference in attenuation between vessel type. As the spatial profile of the pulse wave amplitude distribution is influenced by the point of maximum pulsation within a vessel, a linear mixed random intercept-random slope model with interaction effects was used to analyze the correlations of both the HRW_a and individual trigonometric harmonic coefficients [cosine (a_n), sine (b_n)] of the first and second harmonics [cosine ($a_{n1,2}$) and sine ($b_{n1,2}$)] with the predictors, both the distance along the vessel (V_{dist}) and ophthalmodynamometric force (ODF). A p-value of <0.05 was considered statistically significant for all analyses [63, 64].

To account for the variances of each of the random factors and the residual variance in the structure of the linear mixed effect model, fit statistics was assessed using conditional R^2, which describes the proportion of variance explained by all factors in the model including the predictors V_{dist} and ODF and random factors (subject, age, gender, laterality "right/left", hemiretinal location "superior/inferior"), whereas marginal R^2 describes the proportion of variance explained by the predictors V_{dist} and ODF alone [65]. Multivariate coefficient effect size was calculated for the terms in the interaction model using standardized weighted (β_σ) coefficients [66]. In all regression models the coefficients were reported ±standard error. The 95% confidence intervals were calculated for all regression coefficients.

Results

From a sample of sixteen subjects (8 male and 8 female), a total of 28 eyes were examined. The median age was 48 years (range = 22-69 years). The distribution of the HRW_a was skewed to the right (skewness = 1.58 and 2.03, kurtosis = 3.35 and 4.44) for both the retinal arteries and veins respectively (Fig 4). The median HRW_a in the venous system was 5.11 (range = 0.16–56.6, IQR = 7.64), compared to the arterial system 3.36 (range = 0.20–28.54, IQR = 3.28), the difference between the median values was statistically significant ($p<0.00001$).

Due to the non-normal distribution of the HRW_a in the venous and arterial systems, logarithmic transformation was performed (skewness $logHRW_{a\text{-arterial}} = -0.21$, $logHRW_{a\text{-venous}} = 0.20$), normal quantile-quantile plots (q-q plots) in Fig 5 demonstrated a favorable approximation of the residuals to a normal distribution. The mean logarithmically transformed ±standard error of the mean (SEM) HRW_a was greater in the venous system 0.84±0.034 (95% confidence interval (CI) = 0.77–0.92), than the arterial system 0.65±0.025 (95% CI = 0.60–0.70).

The retinal vascular pulse attenuation was estimated by calculating the regression coefficients correlating log HRW_a and V_{dist}. A higher attenuation was seen in the venous system -0.40±0.065/DD, (p-value < 0.00001, 95% confidence interval -0.53 to -0.27) as opposed to the arterial system -0.17±0.048/DD, (p-value < 0.0004, 95% CI = -0.27 to -0.08). The difference in the attenuation coefficients was compared using ANOVA and was found to be statistically significant (F-statistic = 10751.3, $p<0.0001$). In contrast to the attenuation of HRW_a with distance along the vessel (V_{Dist}), there was an increase of the log HRW_a with ODF by 0.00099 ±0.0005/g force, (p-value<0.03 95% confidence interval 0.000091 to 0.0019) in the venous system. In the arterial system a coefficient of 0.00041±0.0003/g force failed to achieve statistical significance (p-value <0.21, 95% CI = -0.00024 to 0.0011), (Fig 6).

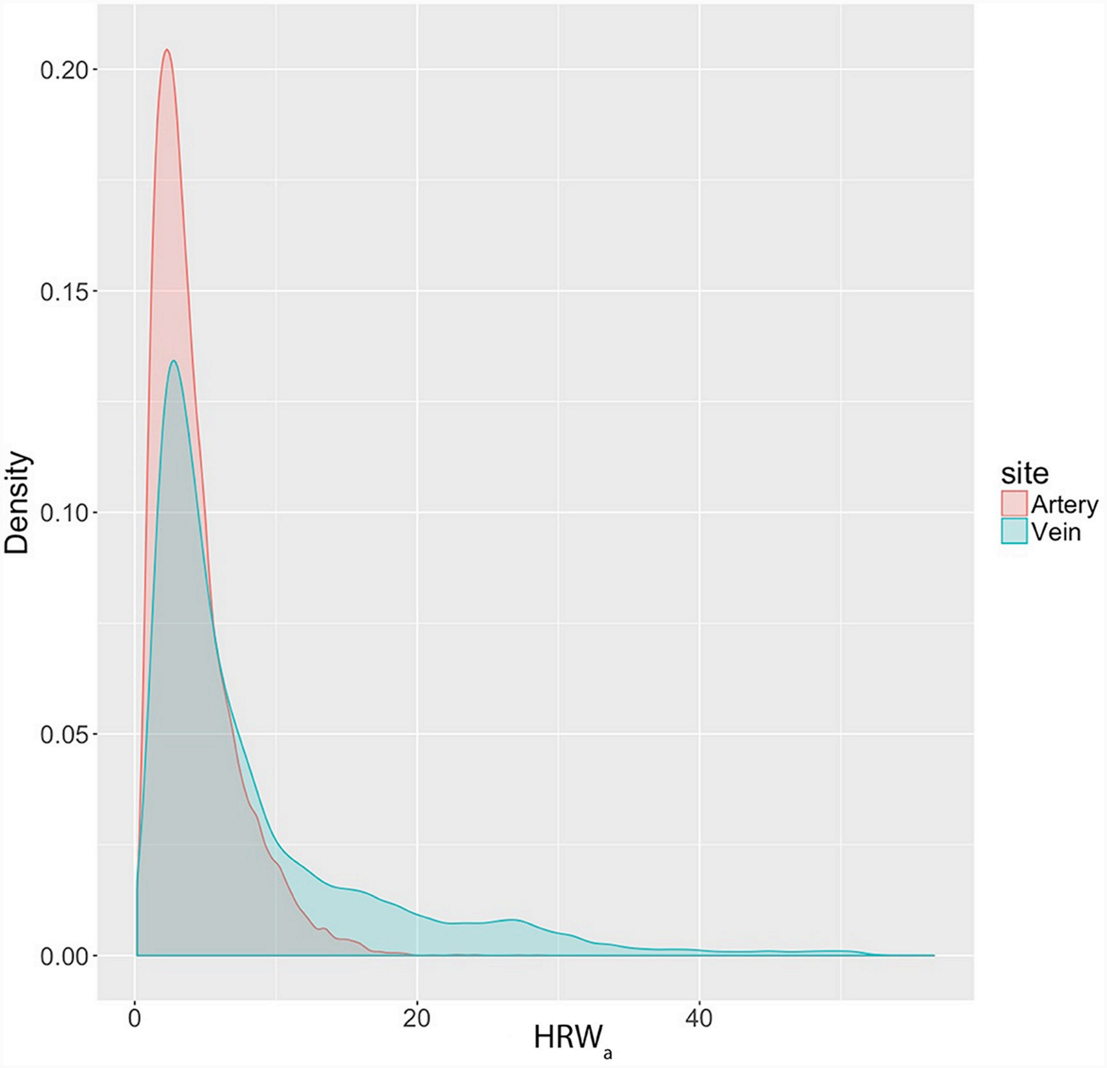

Fig 4. Density plot of the harmonic regression wave amplitude (HRW_a) distribution in the retinal vascular system. The distribution of the HRW_a is non-normal, demonstrating a right skew in both retinal vascular systems. A larger skew in the HRW_a distribution is demonstrated from values from the retinal veins compared to the retinal arteries.

https://doi.org/10.1371/journal.pone.0232523.g004

The equations of the regression lines from Fig 6 can be derived from these correlations:

$$logHRW_{a-venous} = 1.012 - 0.40 \cdot V_{\mathrm{Dist}} \tag{9}$$

$$logHRW_{a-venous} = 0.738 + 0.00099 \cdot ODF \tag{10}$$

$$logHRW_{a-arterial} = 0.713 - 0.17 \cdot V_{\mathrm{Dist}} \tag{11}$$

$$logHRW_{a-arterial} = 0.599 + 0.00041 \cdot ODF \tag{12}$$

The interaction (inter-dependence) of the predictors (V_{dist} and ODF) in estimating the outcome (log HRW_a) are demonstrated in the Figs 7 and 8 for the retinal veins and arteries

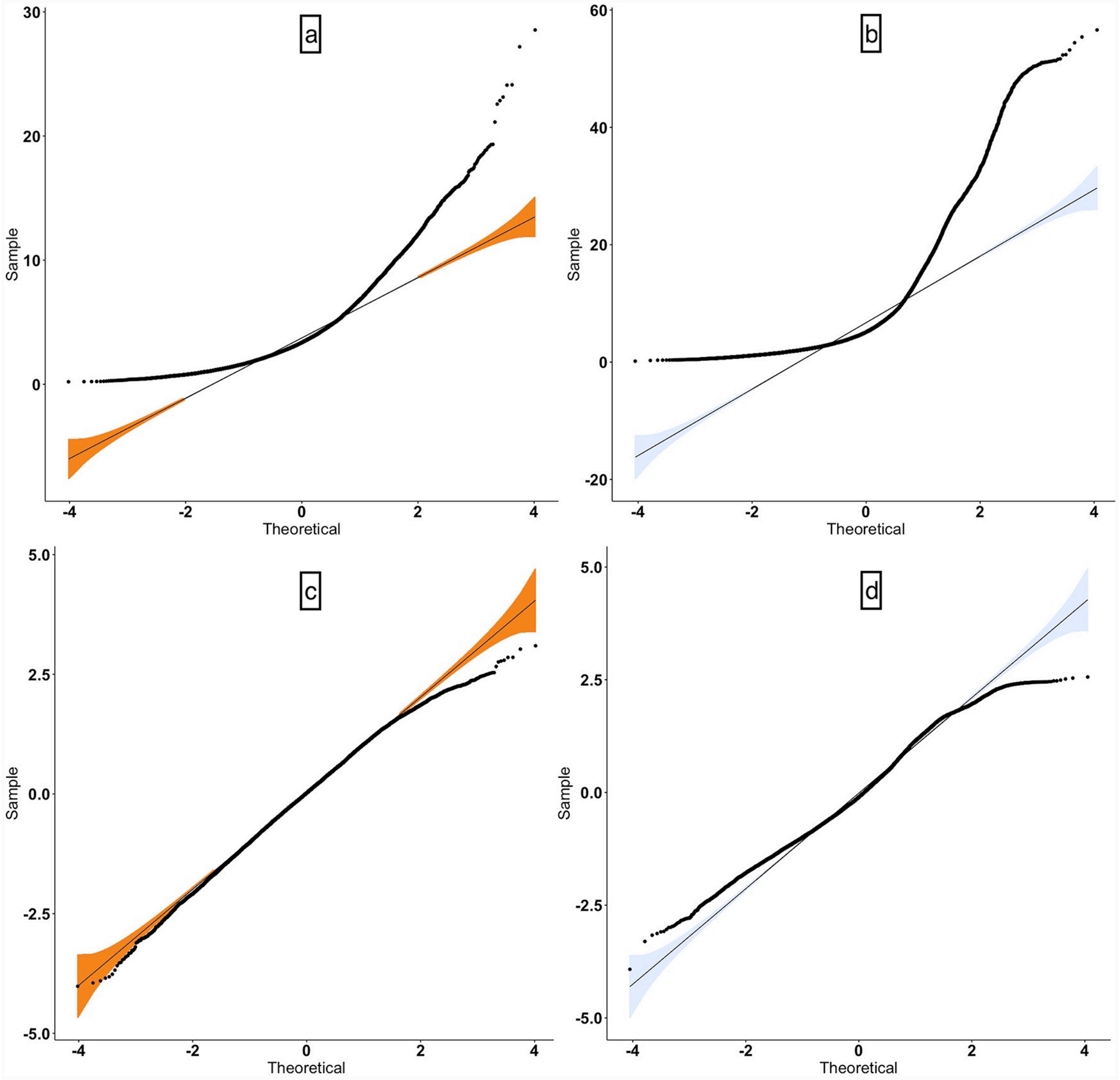

Fig 5. Normal quantile-quantile plot (q-q plot). A normal q-q plot is a graph of the sets of quantiles of the dataset plotted against the quantiles of a normal distribution. The upper row (a,b) represents non-transformed and the right (c,d) logarithmically transformed harmonic regression wave amplitude (HRW_a). There is an improved approximation to a normal distribution after transformation.

https://doi.org/10.1371/journal.pone.0232523.g005

respectively. The interaction model yields the following regression equations:

$$logHRW_{a-venous} = 0.90 - 0.34 \cdot V_{\mathrm{Dist}} + 0.0015 \cdot ODF - 0.00084 \cdot V_{\mathrm{Dist}} \cdot ODF \quad (13)$$

$$logHRW_{a-arterial} = 0.66 - 0.13 \cdot V_{\mathrm{Dist}} + 0.0007 \cdot ODF - 0.0005 \cdot V_{\mathrm{Dist}} \cdot ODF \quad (14)$$

The interaction model coefficients, p-values and standardized (β_σ) coefficients are summarized in Table 1, from which the following conclusions could be drawn: 1) although more than 60% of the variance was explained by the combined predictors and the random factors of the model (conditional R^2), the tested predictors alone accounted for less than 21% of the variance

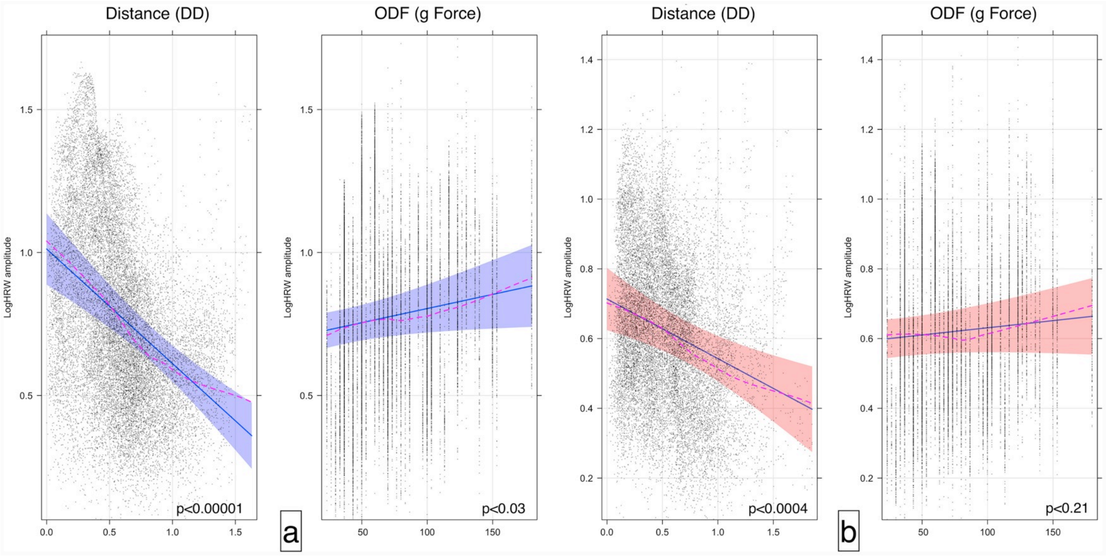

Fig 6. Effect plots of the retinal vascular system. Effect plot of the retinal veins (a) and retinal arteries (b) highlighting the correlation between the vascular pulse wave log harmonic regression waveform amplitude (HRW_a), distance along the vessel from the center of the optic disc (V_{Dist}) in disc diameter and ophthalmodynamometric force (ODF) in grams force (g). Noted is the attenuation of the HRW_a with distance compared to the amplification by ODF. Demonstrated are the 95% confidence intervals for the slope and intercept of the regression line. The dashed line is the loess smoothed regression curve, superposition of both the curve and the regression line indicates a favorable model fit.

https://doi.org/10.1371/journal.pone.0232523.g006

(marginal R^2). 2) There was an attenuation of the HRW_a with V_{Dist} and amplification with ODF as evidenced by a negative coefficient for distance (C_{VD}) and a positive coefficient for ODF (C_{ODF}), respectively, of which both coefficients were higher in the veins compared to the arteries. The standardized β_σ coefficients ($\beta_{\sigma VD}$ and $\beta_{\sigma ODF}$) seen in Table 1 demonstrated this relationship. 3) From the interaction plots in Figs 7 and 8 it can be noted that the slope of the attenuation with V_{Dist} is more negative with increasing ODF. This could be quantified by the negative interaction term (C_{VD^*ODF}). In both vascular systems this change is maximal at the center of the optic disc and reduces towards the retinal periphery.

The influence of ODF on the $logHRW_a$ spatial distribution profile in the vessel wall and the point of maximum pulsation ($logHRW_{amax}$) is demonstrated in a single vascular segment from a test subject in Fig 9, also demonstrated graphically from a single point in the retinal veins and arteries in Figs 10 and 11 respectively. From the total of 36,619 data points, $logHRW_{amax}$ for each vascular segment ($n_{total} = 274$, $n_{arterial} = 138$, $n_{venous} = 136$) was analyzed at different ODF values, a correlation between the distance of shift in $logHRW_{amax}$ measured from the center of the optic disc with changing ODF failed to achieve statistical significance ($p = 0.08, 0.9$) for both the venous and arterial systems respectively.

The Fourier series coefficients (a_n and b_n) for the first and second harmonics

The merits of the coefficient sub-analysis are apparent from Eq 6, as the aim of the study was to investigate amplitude distribution of the HRW in the retinal vascular system, the sub-analysis aimed at investigating if a particular trigonometric wave subset had a favorable correlation with both V_{Dist} and ODF. Table 2 summarizes the numerical statistical properties of the

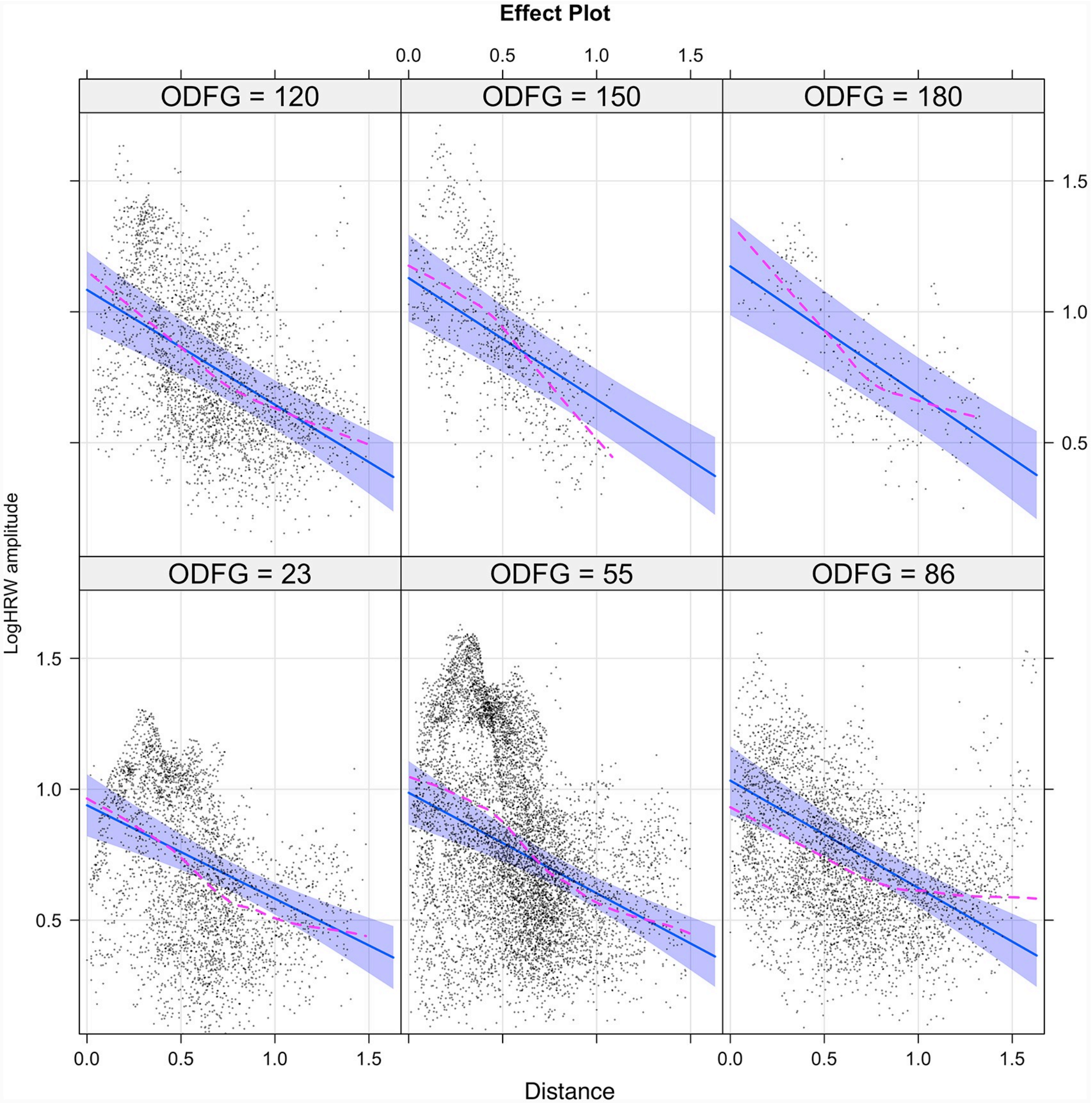

Fig 7. The interaction model of retinal venous pulse log harmonic regression waveform amplitude (logHRW$_a$). There was a positive correlation between HRW$_a$ attenuation and increasing ODF characterized by steepening of the slope of the regression line from -0.36 at 23g force to -0.49 at 180g force with the maximal change in logHRW$_a$ occurring at the center of the optic disc. Demonstrated are the 95% confidence intervals for the slope of the regression line. The sequence commences from the lower left to the upper right. The dashed line is the loess smoothed regression curve, superposition of both the curve and the regression line indicated a favorable model fit.

https://doi.org/10.1371/journal.pone.0232523.g007

coefficients for the first and second harmonics, which are summarized graphically in Fig 12. In addition to the opposed mean coefficient values of a_n and b_n within the individual harmonics seen in this figure, a disproportionate contribution from the a_{n1} coefficient to the first Fourier harmonic was noted in the retinal venous system.

The results of the correlation between the cosine (a_n) and sine (b_n) components of the trigonometric series with the predictors V_{dist} and ODF are summarized in Table 3, which demonstrated a statistical significance for the correlation with V_{dist} was achieved for all coefficients except the b_{n2} coefficient, in contrast to ODF which failed to achieve statistical significance

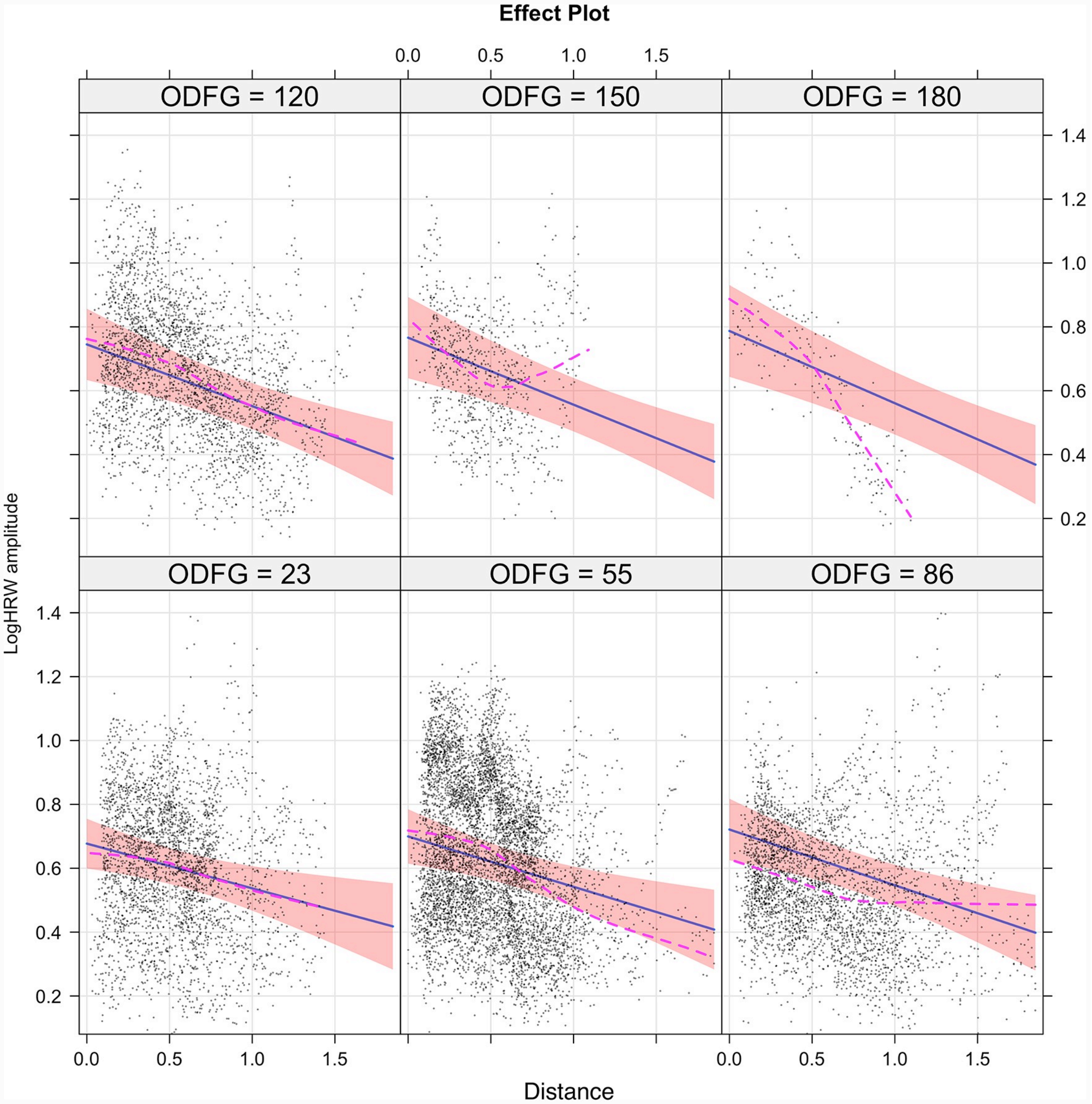

Fig 8. The interaction model of retinal arterial pulse log harmonic regression waveform amplitude (logHRW$_a$). There was a positive correlation between HRW$_a$ attenuation and increasing ODF characterized by steepening of the slope of the regression line from -0.14 at 23g force to -0.23 at 180g force with the maximal change in log HRW$_a$ occurring at the center of the optic disc. Demonstrated are the 95% confidence intervals for the slope of the regression line. The sequence commences from the lower left to the upper right. The dashed line is the loess smoothed regression curve, superposition of both the curve and the regression line indicated a favorable model fit.

https://doi.org/10.1371/journal.pone.0232523.g008

with all but the a_{n1} coefficient. Therefore, among the coefficients there exists varying correlation with the predictors, with the a_{n1} coefficient the strongest and the b_{n2} the weakest linear correlation for both predictors in both retinal vascular systems.

Discussion

Using mPPG, we described the HRW$_a$ distribution and attenuation characteristics of its pulsatile component in both retinal vascular systems non-invasively. The median HRW$_a$ was found to be higher in the retinal veins than in the retinal arteries. This is consistent with clinical

Table 1. Linear mixed effects model with interaction of the predictors.

Interaction Model Parameters		Retinal Vessels			
		Veins	95%CI	Arteries	95%CI
Model Variance	Conditional R^2	0.66		0.63	
	Marginal R^2	0.21		0.06	
Model Coefficient±SEM	I_0	$0.90\pm0.06^{***}$	0.78 to 1.02	$0.66\pm0.04^{***}$	0.58 to 0.74
	C_{VD}	$-0.34\pm0.07^{***}$	-0.47 to -0.21	$-0.13\pm0.05^{*}$	-0.24 to -0.03
	C_{ODF}	$0.0015\pm0.0005^{**}$	0.0005 to 0.002	$0.0007\pm0.001^{*}$	0.0001 to 0.00003
	C_{VD^*ODF}	$-0.00084\pm0.0002^{***}$	-0.001 to-0.0005	$-0.0005\pm0.0001^{***}$	-0.002 to -0.0008
Standardized (β_σ) Coefficient	$\beta_{\sigma VD}$	-0.32 ± 0.06		-0.18 ± 0.07	
	$\beta_{\sigma ODF}$	0.15 ± 0.05		0.11 ± 0.05	
	$\beta_{\sigma VD\cdot ODF}$	-0.086 ± 0.02		-0.086 ± 0.02	

Interaction model coefficients ±standard error (SE) and p-values calculated from of the linear mixed effects model with interaction of the predictors estimating $\log HRW_a$. Distance along the vessel (V_{dist}) in disc diameter and ophthalmodynamometric force (ODF) in grams force (g). I_0 = model intercept, C_{VD} = coefficient of V_{dist},C_{ODF} = coefficient of ODF and C_{VD^*ODF} = coefficient of the interaction term V_{dist}:ODF. Multivariate coefficient effect size is calculated for the terms in the interaction model using standardized Beta coefficients ($\beta_{\sigma n}$) expressed in units of standard deviation, where $\beta_{\sigma VD}$, $\beta_{\sigma ODF}$ and $\beta_{\sigma VD\cdot ODF}$ are the effect sizes for C_{VD}, C_{ODF} and C_{VD^*ODF} respectively. Conditional R^2 = Total explanatory power, Marginal R^2 = Predictor explanatory power.

*** = $p<0.00001$,

** = $p<0.002$,

* = $p<0.05$.

https://doi.org/10.1371/journal.pone.0232523.t001

observations of the retinal venous pulse being visible compared to the arterial pulse in the physiological state [6, 33]. Although the spontaneous venous pulse has been classically described as a binary clinical sign (either present or absent) [6], we demonstrated that modified photo-plethysmography can potentially provide a predictable and quantifiable measurement of the pulse amplitude attenuation. From our previous work, we compared subjective retinal venous pulsation detection with mPPG, the minimum detectable threshold was found to be 5 units (95% confidence interval 4.3 to 6.0) and the area under the receiver operator curve (AU-ROC) was 0.89, which indicated a high accuracy in the detection of pulsatile vascular segments [53]. The reproducibility of this technique demonstrated a coefficient of variation of 13% for vessel pulsation amplitude and 4% for pulsation timing [48]. We are unaware of any other studies in the literature to date that have provided this comparison.

Although it is difficult to detect retinal arterial pulsations clinically, with mPPG we were able to detect the attenuation of the arterial pulse wave at low ODF values and, although the amplification with ODF did not achieve statistical significance (Fig 6), a strong negative linear correlation was detected with V_{Dist}. When this attenuation was compared between both vascular systems, we found the attenuation of the pulse wave in the venous system was almost twice that of the arterial attenuation. Several factors contribute to this phenomenon: vessel wall pulse wave attenuation occurs as a consequence of blood viscosity, the transmission of energy to tissues surrounding the blood vessel, pressure wave reflection particularly at the microvascular bed and most significantly the viscoelasticity of the vessel walls [67–70]. The original work demonstrating the significance of vessel wall viscoelasticity on pulse wave attenuation was derived from experimental and theoretical models of pulse wave propagation [71–73]. The first prediction of attenuation of propagated waves was made by Bergel from the measurement of complex elastic properties of excised vessels [74, 75]. This was followed by a series of theoretical and experimental in vivo and in vitro studies, which mainly compared the linearized and non-linearized equations in the prediction of the propagation constant, which allowed

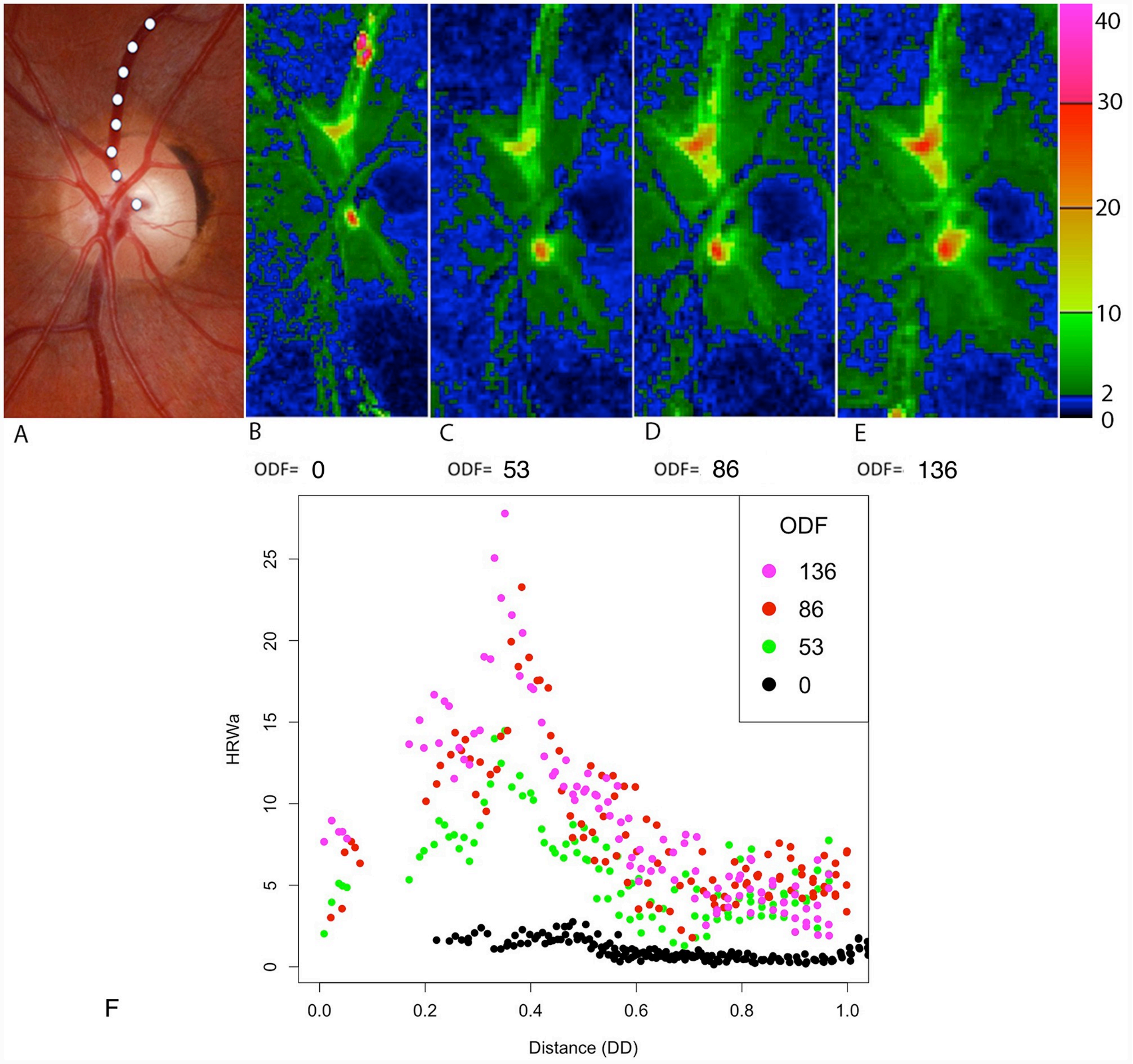

Fig 9. Composite image from a single subject. The distribution of the harmonic regression waveform amplitude (HRW_a) along the retinal vascular tree for three consecutive cardiac cycles at four ODF values (grams force). (A) Color fundus photograph highlighting the vessel from which graph (F) is compiled for the superior temporal retinal vein as indicated by the white dotted line. (B-E) Heat map representation. Note the increase in the HRW_a with increasing ophthalmodynamometric force and the decay as a function of distance in the retinal veins. (F) Scatterplot of the superior retinal vein demonstrating a constant the point of maximum pulsation, in this case 0.38 disc diameter from the optic disc. DD = Disc diameter.

https://doi.org/10.1371/journal.pone.0232523.g009

attenuation to be expressed in terms of percentage transmission through the systemic vessels as outlined in Table 4.

A discrepancy between the propagation attenuation coefficient (α) predicted by the theoretical and the experimental models, inexplicable by that derived from the viscosity of blood alone, lead to the conclusion by McDonald et al. of the contribution of vessel wall viscoelasticity being the major factor accounting for pulse wave attenuation [72, 73]. This was

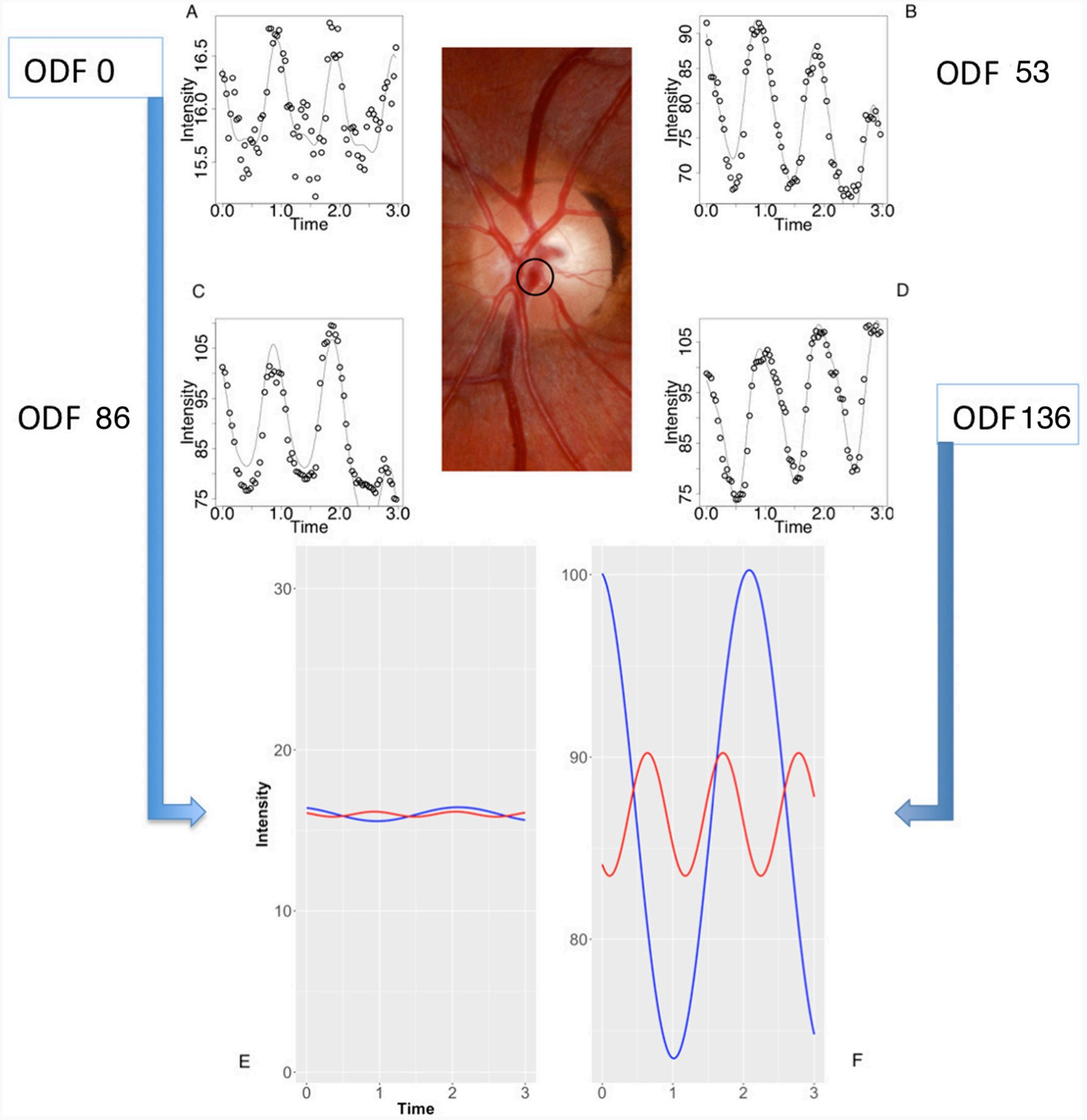

Fig 10. Composite image from the subject from Fig 9. (A-D) The retinal venous pulse harmonic regression waveforms are represented graphically for ophthalmodynamometric force (ODF) 0, 53, 86 and 136 grams force. (E-F) The decomposed first (blue line) and second (red line) Fourier harmonic waves at ODF = 0 at (E) and ODF = 136 grams force at (F) calculated from the Fourier series equation for a single point as highlighted in the central color fundus image. Noted were the increase in the amplitude of the waveforms and the increase in the y-intercept of the regression line with increasing ODF.

https://doi.org/10.1371/journal.pone.0232523.g010

demonstrated in subsequent studies, particularly in those studies that analyzed the linearized models of pulse propagation attenuation [70]. Classical elasticity theory is based on an assumption that material is both homogenous and isotropic; however, in biological tissues, particularly in the walls of blood vessels, which are neither homogenous nor isotropic, this assumption is violated. Therefore, vascular distensibility (change in cross-sectional area for a change in pressure) and compliance (change in volume for a change in pressure) both have non-linear dimension-pressure responses [20, 82]. In the systemic vessels the difference in the vessel wall structure, accounts for a difference in viscoelastic responses between the arteries

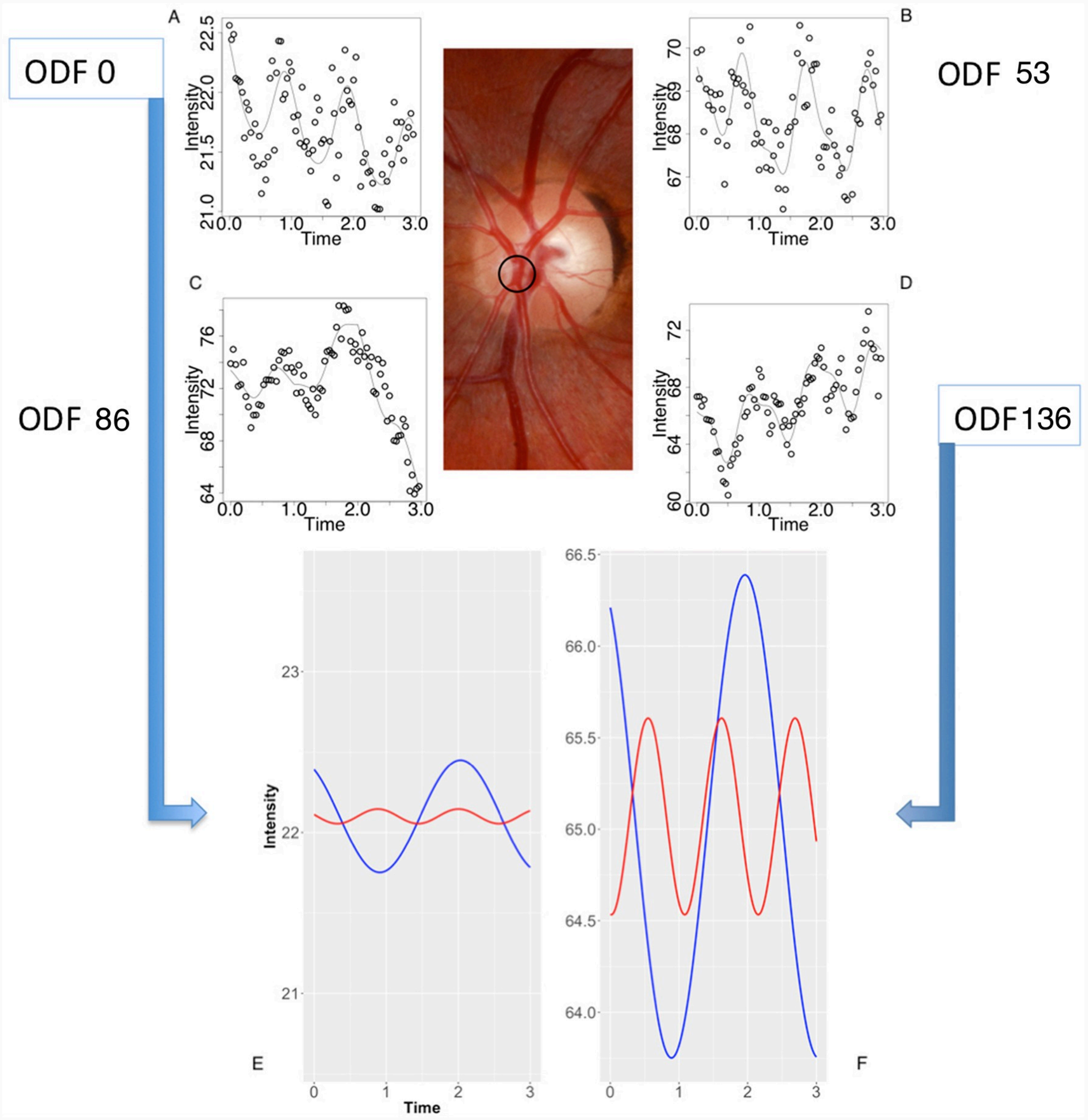

Fig 11. Composite image from the subject from Fig 9. (A-D) The retinal arterial pulse harmonic regression waveforms are represented graphically for ophthalmodynamometric force (ODF) 0, 53, 86 and 136 grams force. (E-F) The decomposed first (blue line) and second (red line) Fourier harmonic waves at ODF = 0 at (E) and ODF = 136 grams force at (F) calculated from the Fourier series equation for a single point as highlighted in the central color fundus image. Noted were the increase in the amplitude of the waveforms and the increase in the y-intercept of the regression line with increasing ODF.

https://doi.org/10.1371/journal.pone.0232523.g011

and the veins. The vessel wall consists mainly (70%) of water, with the rest comprised of a material that determines elastic properties (collagen, elastin and smooth muscle) [19]. Consequently, measured arterial compliance curves are curvilinear [83] whereas in the veins this relationship is sigmoidal [84], resulting in a difference in systemic venous compliance being 19 to 24 times of the arterial for an identical transmural pressure and cross-sectional area [82, 85–87]. In the retinal microvascular system, this relationship has not been investigated, however, ultrastructural differences in the vessel walls are well recognized, whereas the retinal arteries are devoid of elastin and consist mainly of layers of collagen with smooth muscle layers, the

Table 2. Dispersion and central tendency of the coefficients of the first two harmonics of the retinal arteries and veins.

	Range	Median	IQR	Skewness	Kurtosis
Retinal Veins					
a_{n1}	-16.08 to 23.38	0.93	2.52	1.97	4.79
b_{n1}	-14.99 to 12.76	-0.81	1.89	-1.16	1.62
a_{n2}	-8.75 to 5.39	-0.24	0.82	-1.40	3.96
b_{n2}	-8.10 to 9.74	0.09	0.72	0.14	5.51
Retinal Arteries					
a_{n1}	-5.93 to 9.73	0.52	1.24	0.94	3.61
b_{n1}	-10.02 to 8.01	-0.75	1.38	-0.61	2.71
a_{n2}	-6.08 to 4.85	-0.11	0.54	-0.20	7.71
b_{n2}	-3.85 to 5.09	0.11	0.56	1.01	3.58

There is a higher median pulsation amplitude, skewness and wider range of the coefficients of the retinal veins compared to the retinal arteries. These findings are demonstrated graphically in Fig 12. IQR = interquartile range, $a_{n1,2}$ = cosine coefficients and $b_{n1,2}$ = sine coefficients of the first and second Fourier harmonics respectively.

https://doi.org/10.1371/journal.pone.0232523.t002

retinal veins being comprised solely of layers of pericytes surrounded by a collagenous layer of perivascular tissue [88]. This difference in structure is likely to result in a difference in the vascular dimension-pressure response and thereupon a discrepancy in the slopes of attenuation of the HRW_a between the vessels as seen in Figs 6, 7 and 8.

The ophthalmodynamometer allows a graded compressive force to be applied to the globe, thereby inducing a measured increase in intraocular pressure. This, in turn, steepens the pressure gradient between the intraocular and retro-ocular compartments and leads to an amplification of retinal vascular pulsations [89, 90]. This sequence was detailed from a single subject in Figs 9 to 11. However, the increase in the slope of the regression line (becoming more negative) with increasing ODF as seen in Figs 7 and 8 and the negative values in the interaction terms in Eqs 13 and 14 involve complex hemodynamic mechanisms, which are poorly understood. Theoretical [91] and experimental models [92–94] have attempted to investigate the retinal and retrobulbar hemodynamic changes from induced IOP elevation. Harris et al. using color doppler imaging, reported changes in the central retinal artery (CRA) including reduced peak systolic velocity, end-diastolic velocity and an increase in the resistive index. Using a method combining Doppler sonography with laser interferometry, Findl et al. concluded that a reduction in the choroidal blood flow in response to an induced increase in IOP was the reason behind a measured reduction in fundus pulsations at the macula and optic disc. Neither investigators detected changes in the hemodynamics of the ophthalmic artery [92, 93]. Therefore an increase in compliance in both the retinal arteries and the retinal veins consequent to a reduction in CRA and possibly choroidal blood flow may be a reason behind the steepening of the regression line with increase ODF observed in Figs 7 and 8. These results are influenced by other systemic factors on the IOP/ocular hemodynamic relationship, including arterial blood pressure, cerebrospinal fluid pressure, orbital tissue pressure, the pressure in the cavernous sinus blood flow, auto-regulation and ocular biomechanics [50], which may make our results difficult to generalize to a wider population.

Lam et al. reported a strong relationship between venous pulsation amplitude with increasing venous diameter, decreasing absolute cup margin distance and decreasing tissue depth overlying the vein [90]. In our subjects the location of the point of maximum venous pulsation,

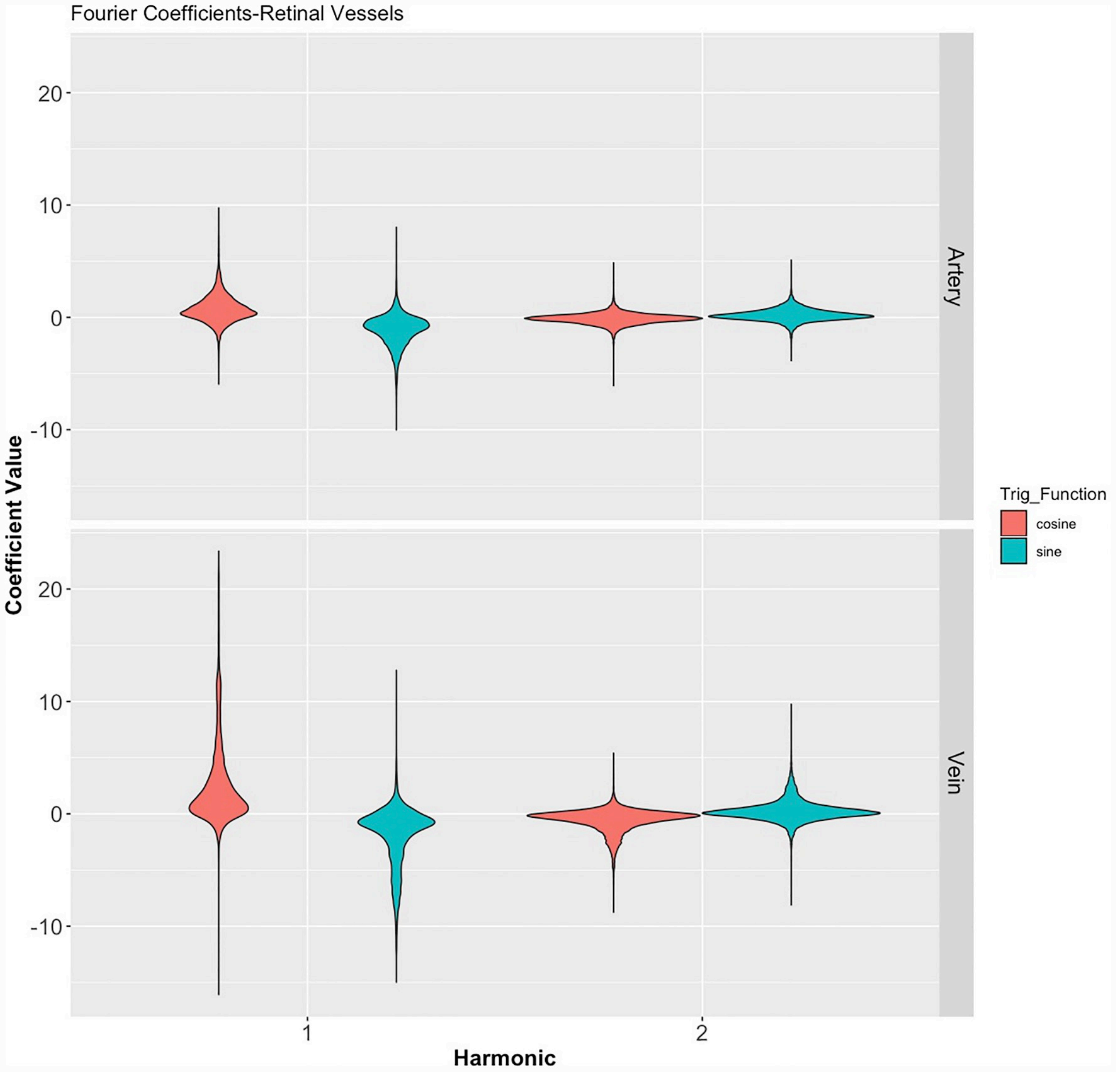

Fig 12. Violin plot of the distribution of the Fourier coefficients of the first and second Fourier harmonics in both vascular systems classified by trigonometric function. Demonstrating the wider range for both the cosine (a_n) and sine (b_n) coefficients in the veins, a narrower dispersion of values for the second Fourier harmonics and the disparate distribution, with displacement in the opposite direction across the axis of reference between the a_n and b_n coefficients in both vascular systems. Numeric values of the figure are outlined in Table 2.

https://doi.org/10.1371/journal.pone.0232523.g012

therefore, may be determined by these anatomic characteristics. We found a constant location of the point of maximum venous pulsation in the retinal veins with increasing ODF. To interpret this finding, it is important to consider some of the physiologic mechanisms of the spontaneous venous pulse (SVP). In simplest terms, a variation in the pressure gradient as the vein traverses the lamina cribrosa is the cause of the SVP [95]. However, the spatial distribution of the pulse amplitude along the vein involves a more complex relationship best described by a Starling resistor, which is defined as a collapsible tube in which the pressure external to the tube exceeds the outflow pressure. It predicts that pulsation amplitude is highest near the Starling resistor exit and is attenuated upstream towards the inlet region, this model predicts an expansion of the zone and a constancy of the maximal point of deformation in the wall of the resistor with increasing external force (Fig 9A–9D) [13, 96, 97].

Table 3. Linear mixed effects model of the individual coefficients of the Fourier trigonometric series from the first and second harmonics.

	Coefficient Distance	95% CI	p-value	Coefficient ODF	95% CI	p-value
			Retinal Veins			
a_{n1}	-3.79±0.78	-5.320 to -2.268	0.000001	0.026±0.0099	0.006 to 0.045	0.01
b_{n1}	1.98±0.48	1.033 to 2.93	0.00004	0.00083±0.003	-0.005 to 0.007	0.8
a_{n2}	0.498±0.13	0.249 to 0.747	0.0001	-0.005±0.003	-0.01 to 0.0009	0.1
b_{n2}	-0.0037±0.17	-0.337 to 0.331	1	-0.004±0.002	-0.008 to 0.0009	0.1
			Retinal Arteries			
a_{n1}	-1.27±0.37	-1.992 to -0.549	0.0006	0.009±0.04	0.002 to 0.02	0.01
b_{n1}	1.026±0.22	0.591 to 1.463	0.000004	-0.0002±0.002	-0.004 to 0.004	0.93
a_{n2}	0.21±0.076	0.047 to 0.348	0.01	-0.002±0.002	-0.005 to 0.00091	0.2
b_{n2}	-0.041±0.16	-0.347 to 0.267	0.81	-0.0007±0.001	-0.0032 to 0.0021	0.58

Linear mixed effect model correlating the Fourier coefficients (coefficient value±standard error) with distance along the vessel (V_{Dist}) and ophthalmodynamometric force (ODF) in both retinal veins and arteries. Statistical significance was achieved for the correlation with V_{Dist} for all coefficients except the b_{n2} coefficient. In contrast ODF failed to achieve statistical significance with a ($p < 0.05$) limit with all but the a_{n1} coefficient for both vascular systems. $a_{n1,2}$ = cosine coefficients and $b_{n1,2}$ = sine coefficients of the first and second Fourier harmonics respectively. 95% CI = 95% confidence interval.

https://doi.org/10.1371/journal.pone.0232523.t003

From Eq 6 it is noted that the HRW is a consequence of the summation of the individual trigonometric sine and the cosine waves. The sub-analysis of these individual trigonometric wave coefficients demonstrated that the a_{n1} coefficient in both vascular systems was the only coefficient in the first two harmonics that showed a statistically significant correlation with both predictors (V_{Dist} and ODF). Additionally, this coefficient demonstrated a wider range compared to the sine coefficient to the first harmonic waveform (Fig 12). The reason underpinning the dominance of this waveform is not testable in our current study; however our hypothesis is that this wave may be in phase with the fundamental harmonic of the CSF pulse wave (CSFPW), which is the primary driver for the retinal venous pulse [15]. The fundamental

Table 4. Summary of studies in vascular flow related pulse wave attenuation.

Author	Year	Method	Site	Transmission Range (%)	Frequency Range(Hz)
Womersley	1957 [71]	Theoretical	C	C = 0.99-0.92	C = 2-15
			F	F = 1.0-0.96	F = 2-13
Bergel	1961 [76]	In vitro	A	A = 0.98-0.86	2.5-18
			T	T = 0.97-0.72	2.5-18
			F	F = 0.97-0.84	2.5-18
			C	C = 0.97-0.84	2.5-18
Anliker	1968 [77]	In vivo	T	T = 0.7-0.1*	1-3
Mc Donald	1968 [78]	In vitro	C	C = 0.87-0.75	3-14
Mc Donald	1968 [79]	In vivo	C	C = 0.90-0.81	3-11
Mc Donald	1968 [73]	In vitro	C	C = 0.84-0.60	3-11
Wetterer	1968 [75]	In vivo	C	C = 0.98-0.92	3-15
Li	1981 [80]	In vivo	A, F, C, I	C = 0.89-0.47	1-14
Milnor	1975 [25]	In vivo	F	F = 0.85-0.53	3-12
Milnor	1978 [81]	In vivo	F	F = 0.89-0.5	1-13

Arterial flow wave attenuation using various published models and differing methodologies. Transmission was measured as a function of wave frequency/10 cm vessel length. A = Abdominal aorta, C = Carotid, F = Femoral, T = Thoracic aorta, I = Iliac. The theoretical method was calculated using Womersley's Theory.

* Transmission measured over a 20cm arterial segment. Adapted from McDonald's blood flow in arteries: theoretical, experimental and clinical principles [75].

https://doi.org/10.1371/journal.pone.0232523.t004

harmonic of the CSFPW is derived from the systemic arterial pressure pulse and is therefore the dominant contributor to this pulse waveform [98]. Consequently, the amplitude and the contour of the CSFPW are dependent on the radius of the arterioles and the characteristics of the walls of the vessels in the cerebrovascular bed [98]. We hypothesize that these factors are likely to be the dominant contributors to the fundamental harmonic of the retinal vascular pulse waveform and reflect factors that influence this waveform indirectly.

The limitations of our described technique include a relatively small sample size. Whereas the interaction model described <65% of the variance, the predictors (V_{dist}, ODF) accounted for <20%, with a further 35% was not accounted for in the linear mixed-effects model. A larger sample size would allow assessment of other factors influencing the variance within the model, particularly age. The limits of the sampling frequency (frame rate), determines the number of harmonics extractable from the original signal, a frame rate of 25 FPS allowed correlations to be made on the first two harmonics only. A higher imaging frame rate would theoretically permit the extraction of higher frequency harmonics from the video sequence. Inaccuracies in measuring the pulse amplitude could arise from differences in tissue biomechanics between individuals; furthermore, although baseline intraocular pressure was measured, this was not factored in the analysis. These parameters would influence the ophthalmodynamometric force applied to some extent. Also, transmural pressure is a significant factor governing and linking pulsatile amplitude to intravascular blood flow, as this factor can only be measured invasively, there was no means for this parameter to be factored in our study.

We modeled the attenuation characteristics for the arteries and the veins independently, therefore our work may provide a benchmark for comparison of attenuation characteristics in retinal vascular disease involving the vessel wall. These include age related atherosclerosis [99], hypertension [100], diabetes [101, 102], the influence of pharmacological agents [23] and cerebrospinal fluid pressure dynamics [103, 104].

Conclusion

Retinal vascular pulse HRW_a attenuation was described using modified photo-plethysmography. The predictable attenuation characteristics in normal subjects suggest that this technique may allow the quantification of retinal vascular compliance and other hemodynamic alterations.

Supporting information

S1 Data.
(CSV)

Author Contributions

Conceptualization: Anmar Abdul-Rahman, William Morgan, Dao-Yi Yu.

Data curation: Anmar Abdul-Rahman, William Morgan, Dao-Yi Yu.

Formal analysis: Anmar Abdul-Rahman.

Methodology: Anmar Abdul-Rahman, William Morgan.

Software: Anmar Abdul-Rahman, William Morgan.

Supervision: William Morgan, Dao-Yi Yu.

Validation: Anmar Abdul-Rahman, William Morgan.

Visualization: Anmar Abdul-Rahman.

Writing – original draft: Anmar Abdul-Rahman.

Writing – review & editing: William Morgan, Dao-Yi Yu.

References

1. Salvi P. Evaluation of the mechanical properties of large arteries. In: Pulse Waves. Springer, Milano; 2012. pp. 17–44. https://doi.org/10.1007/978-88-470-2439-7_4
2. Zamir M, Ritman E. Pulsatile Flow In An Elastic Tube. In: The Physics Of Pulsatile Flow. Biological Physics Series. Springer, New York, NY; 2000. pp. 113–145. https://doi.org/10.1007/978-1-4612-1282-9_5
3. Morgan WH, Hazelton ML, Azar SL, House PH, Yu DY, Cringle SJ, et al. Retinal venous pulsation in glaucoma and glaucoma suspects. Ophthalmology. 2004; 111(8):1489–1494. https://doi.org/10.1016/j.ophtha.2003.12.053 PMID: 15288976
4. Balaratnasingam C, Morgan WH, Hazelton ML, House PH, Barry CJ, Chan H, et al. Value of retinal vein pulsation characteristics in predicting increased optic disc excavation. Br J Ophthalmol. 2007; 91(4):441–444. https://doi.org/10.1136/bjo.2006.105338 PMID: 17035270
5. Legler U, Jonas JB. Frequency of spontaneous pulsations of the central retinal vein in glaucoma. J Glaucoma. 2009; 18(3):210–212. https://doi.org/10.1097/IJG.0b013e318182edd2 PMID: 19295374
6. Jacks A, Miller N. Spontaneous retinal venous pulsation: aetiology and significance. J Neurol Neurosurg Psychiatry. 2003; 74(1):7–9. https://doi.org/10.1136/jnnp.74.1.7 PMID: 12486256
7. Hedges TR, Baron EM, Sinclair SH. The retinal venous pulse: its relation to optic disc characteristics and choroidal pulse. Ophthalmology. 1994; 101(3):542–547. https://doi.org/10.1016/S0161-6420(94)31302-9 PMID: 8127575
8. Jonas JB. Ophthalmodynamometric measurement of orbital tissue pressure in thyroid-associated orbitopathy. Acta Ophthalmol (Copenh). 2004; 82(2):239–239. https://doi.org/10.1111/j.1600-0420.2004.00150a.x
9. Jonas JB. Ophthalmodynamometric assessment of the central retinal vein collapse pressure in eyes with retinal vein stasis or occlusion. Graefes Arch Clin Exp Ophthalmol. 2003; 241(5):367–370. https://doi.org/10.1007/s00417-003-0643-7 PMID: 12698255
10. Jonas JB, Harder B. Ophthalmodynamometric differences between ischemic vs nonischemic retinal vein occlusion. Am J Ophthalmol. 2007; 143(1):112–116. https://doi.org/10.1016/j.ajo.2006.09.019 PMID: 17101111
11. Do H, Kang HK, Beaumont PE. Prognostic Significance of Ophthalmodynamometry in Central Retinal Vein Occlusion. Proceedings of the 10th Annual Conference of the Association for Research in Vision and Ophthalmology; 2008 May 18-20; Fort Lauderdale, Florida. Investig Ophthalmol Vis Sci; 49(13):5438–5438. Available from: https://iovs.arvojournals.org/article.aspx?articleid=2380819.
12. McAllister IL, Tan MH, Smithies LA, Wong WL. The effect of central retinal venous pressure in patients with central retinal vein occlusion and a high mean area of nonperfusion. Ophthalmology. 2014; 121(11):2228–2236. https://doi.org/10.1016/j.ophtha.2014.05.031 PMID: 25037752
13. Morgan WH, Hazelton ML, Yu DY. Retinal venous pulsation: Expanding our understanding and use of this enigmatic phenomenon. Prog Retin Eye Res. 2016; 55:82–107. https://doi.org/10.1016/j.preteyeres.2016.06.003 PMID: 27417037
14. Jonas JB, Wang N, Xu J, Wang YX, You QS, Yang D, et al. Diabetic retinopathy and estimated cerebrospinal fluid pressure. The Beijing Eye Study 2011. PLoS One. 2014; 9(5):e96273. https://doi.org/10.1371/journal.pone.0096273 PMID: 24789334
15. Morgan WH, Lind CR, Kain S, Fatehee N, Bala A, Yu DY. Retinal Vein Pulsation Is in Phase with Intracranial Pressure and Not Intraocular Pressure. Investig Ophthalmol Vis Sci. 2012; 53(8):4676–4681. https://doi.org/10.1167/iovs.12-9837
16. Moxham I. Understanding Arterial Pressure Waveforms. South Afr J Anaesth. Analg. 2003; 9(1):40–42. https://doi.org/10.1080/22201173.2003.10872991
17. Farrow RL, Stacy RW. Harmonic analysis of aortic pressure pulses in the dog. Circ Res. 1961; 9(2):395–401. https://doi.org/10.1161/01.res.9.2.395 PMID: 13698288
18. Vlachopoulos C, O'Rourke M, Nichols WW. Properties of the arterial wall: practice. In: McDonald's blood flow in arteries: theoretical, experimental and clinical principles. CRC press, Taylor & Francis Group, Florida, United States; 2011. pp. 77–109.

19. Caro CG, Pedley TJ, Schroter RC, Seed WA, Parker KH. Solid mechanics and the properties of blood vessel walls. In: The mechanics of the circulation. 2nd ed. Cambridge: Cambridge University Press; 2012. pp. 86–104. https://doi.org/10.1017/CBO9781139013406

20. Li JK. Physical concepts and basic fluid mechanics. In: Dynamics of the vascular system. Vol 1. World Scientific Publishing Co Pte Ltd, Singapore; 2004. pp. 41–75. https://doi.org/10.1142/9789812562661_0003

21. Tozzi P, Corno A, Hayoz D. Definition of arterial compliance. Am J Physiol Heart Circ Physiol. 2000; 278(4):1407. https://doi.org/10.1152/ajpheart.2000.278.4.H1407

22. Caro CG, Pedley TJ, Schroter RC, Seed WA, Parker KH. The systemic arteries. In: The mechanics of the circulation. 2nd ed. Cambridge: Cambridge University Press; 2012. pp. 238–342. https://doi.org/10.1017/CBO9781139013406

23. Glasser SP, Arnett DK, McVeigh GE, Finkelstein SM, Bank AJ, Morgan DJ, et al. Vascular compliance and cardiovascular disease: a risk factor or a marker? Am J Hypertens. 1997; 10(10):1175–1189. https://doi.org/10.1016/s0895-7061(97)00311-7 PMID: 9370391

24. Hainsworth R. The importance of vascular capacitance in cardiovascular control. Physiology. 1990; 5 (6):250–254. https://doi.org/10.1152/physiologyonline.1990.5.6.250

25. Milnor WR, Nichols WW. A new method of measuring propagation coefficients and characteristic impedance in blood vessels. Circ Res. 1975; 36(5):631–639. https://doi.org/10.1161/01.res.36.5.631 PMID: 1091370

26. Kotliar KE, Baumann M, Vilser W, Lanzl IM. Pulse wave velocity in retinal arteries of healthy volunteers. Br J Ophthalmol. 2011; 95(5):675–679. https://doi.org/10.1136/bjo.2010.181263 PMID: 21041458

27. Kotliar K, Hanssen H, Eberhardt K, Vilser W, Schmaderer C, Halle M, et al. Retinal pulse wave velocity in young male normotensive and mildly hypertensive subjects. Microcirculation. 2013; 20(5):405–415. https://doi.org/10.1111/micc.12036 PMID: 23289749

28. Golzan SM, Butlin M, Kouchaki Z, Gupta V, Avolio A, Graham SL. Characterizing dynamic properties of retinal vessels in the rat eye using high speed imaging. Microvasc Res. 2014; 92:56–61. https://doi.org/10.1016/j.mvr.2013.12.006 PMID: 24389464

29. Seifert BU, Vilser W. Retinal Vessel Analyzer (RVA)-design and function. Biomedizinische Technik/Biomedical Engineering. 2002; 47(s1b):678–681. https://doi.org/10.1515/bmte.2002.47.s1b.678

30. Garhofer G, Bek T, Boehm AG, Gherghel D, Grunwald J, Jeppesen P, et al. Use of the retinal vessel analyzer in ocular blood flow research. Acta Ophthalmol (Copenh). 2010; 88(7):717–722. https://doi.org/10.1111/j.1755-3768.2009.01587.x

31. Chen HC, Patel V, Wiek J, Rassam SM, Kohner EM. Vessel diameter changes during the cardiac cycle. Eye. 1994; 8(1):97. https://doi.org/10.1038/eye.1994.19 PMID: 8013728

32. Kumar DK, Aliahmad B, Hao H, Che Azemin MZ, Kawasaki R. A method for visualization of fine retinal vascular pulsation using nonmydriatic fundus camera synchronized with electrocardiogram. ISRN Ophthalmol. 2013:865834. https://doi.org/10.1155/2013/865834

33. Moret F, Poloschek CM, Lagreze WA, Bach M. Visualization of fundus vessel pulsation using principal component analysis. Invest Ophthalmol Visual Sci. 2011; 52(8):5457–5464. https://doi.org/10.1167/iovs.10-6806

34. Spahr H, Hillmann D, Hain C, Pfäffle C, Sudkamp H, Franke G, et al. Imaging pulse wave propagation in human retinal vessels using full-field swept-source optical coherence tomography. Opt Lett. 2015; 40(20):4771–4774. https://doi.org/10.1364/OL.40.004771 PMID: 26469616

35. Allen J. Photoplethysmography and its application in clinical physiological measurement. Physiol Meas. 2007; 28(3):1–59. https://doi.org/10.1088/0967-3334/28/3/R01

36. Webster JG. Light absorbance in pulse oximetry. In: Design of pulse oximeters. CRC Press, Taylor & Francis Group, Florida, United States; 1997. p. 40–55.

37. Imholz BP, Wieling W, van Montfrans GA, Wesseling KH. Fifteen years experience with finger arterial pressure monitoring: assessment of the technology. Cardiovasc Res. 1998; 38(3):605–616. https://doi.org/10.1016/s0008-6363(98)00067-4 PMID: 9747429

38. Naschitz JE, Bezobchuk S, Mussafia-Priselac R, Sundick S, Dreyfuss D, Khorshidi I, et al. Pulse transit time by R-wave-gated infrared photoplethysmography: review of the literature and personal experience. J Clin Monit Comput. 2004; 18(5-6):333–342. https://doi.org/10.1007/s10877-005-4300-z PMID: 15957624

39. Payne R, Symeonides C, Webb D, Maxwell S. Pulse transit time measured from the ECG: an unreliable marker of beat-to-beat blood pressure. J Appl Physiol. 2006; 100(1):136–141. https://doi.org/10.1152/japplphysiol.00657.2005 PMID: 16141378

40. Romano SM, Pistolesi M. Assessment of cardiac output from systemic arterial pressure in humans. Crit Care Med. 2002; 30(8):1834–1841. https://doi.org/10.1097/00003246-200208000-00027 PMID: 12163802

41. Harms MP, Wesseling KH, Frank P, Jenstrup M, Van Goudoever J, Secher NH, et al. Continuous stroke volume monitoring by modelling flow from non-invasive measurement of arterial pressure in humans under orthostatic stress. Clin Sci. 1999; 97(3):291–301. https://doi.org/10.1042/cs0970291 PMID: 10464054

42. Nitzan M, Babchenko A, Shemesh D, Alberton J. Influence of thoracic sympathectomy on cardiac induced oscillations in tissue blood volume. Med Biol Eng Comput. 2001; 39(5):579–583. https://doi.org/10.1007/bf02345149 PMID: 11712655

43. Nitzan M, Vatine J, Babchenko A, Khanokh B, Tsenter J, Stessman J. Simultaneous measurement of the photoplethysmographic signal variability in the right and left hands. Lasers Med Sci. 1998; 13 (3):189–195. https://doi.org/10.1007/s101030050073

44. Simonson E. Photoelectric plethysmography; methods, normal standards, and clinical application. Geriatrics. 1956; 11(10):425. PMID: 13365918

45. Oliva I, Ipser J, Roztocil K, Guttenbergerova K. Fourier analysis of the pulse wave in obliterating arteriosclerosis. Vasa. 1976; 5(2):95. PMID: 973429

46. Sherebrin M, Sherebrin R. Frequency analysis of the peripheral pulse wave detected in the finger with a photoplethysmograph. IEEE Trans Biomed Eng. 1990; 37(3):313–317. https://doi.org/10.1109/10.52332 PMID: 2329004

47. Betz-Stablein B, Hazelton ML, Morgan WH. Modelling retinal pulsatile blood flow from video data. Stat Methods Med Res. 2016; p. 1575–1584. https://doi.org/10.1177/0962280216665504 PMID: 27587593

48. Morgan WH, Hazelton ML, Betz-Stablein BD, Yu DY, Lind CR, Ravichandran V, et al. Photoplethysmographic measurement of various retinal vascular pulsation parameters and measurement of the venous phase delay. Investig Ophthalmol Vis Sci. 2014; 55(9):5998–6006. https://doi.org/10.1167/iovs.14-15104

49. Westlake WH, Morgan WH, Yu DY. A pilot study of in vivo venous pressures in the pig retinal circulation. Clin Exp Ophthalmol. 2001; 29(3):167–170. https://doi.org/10.1046/j.1442-9071.2001.00399.x PMID: 11446461

50. Jonas J. Reproducibility of ophthalmodynamometric measurements of central retinal artery and vein collapse pressure. Br J Ophthalmol. 2003; 87(5):577–579. https://doi.org/10.1136/bjo.87.5.577 PMID: 12714398

51. Morgan WH, Cringle SJ, Kang MH, Pandav S, Balaratnasingam C, Ezekial D, et al. Optimizing the calibration and interpretation of dynamic ocular force measurements. Graefes Arch Clin Exp Ophthalmol. 2010; 248(3):401–407. https://doi.org/10.1007/s00417-009-1288-y PMID: 20107829

52. R Core Team. R: A Language and Environment for Statistical Computing; 2019. Available from: https://www.R-project.org/.

53. Morgan WH, Abdul-Rahman A, Yu DY, Hazelton ML, Betz-Stablein B, Lind CR. Objective detection of retinal vessel pulsation. PLoS One. 2015; 10(2):e0116475. https://doi.org/10.1371/journal.pone.0116475 PMID: 25643350

54. Zijlstra W, Buursma A, Meeuwsen-Van der Roest W. Absorption spectra of human fetal and adult oxyhemoglobin, de-oxyhemoglobin, carboxyhemoglobin, and methemoglobin. Clin Chem. 1991; 37 (9):1633–1638. https://doi.org/10.1093/clinchem/37.9.1633 PMID: 1716537

55. Mook G, Buursma A, Gerding A, Kwant G, Zijlstra W. Spectrophotometric determination of oxygen saturation of blood independent of the presence of indocyanine green. Cardiovasc Res. 1979; 13(4):233–237. https://doi.org/10.1093/cvr/13.4.233 PMID: 380808

56. Maschal RA Jr, Young SS, Reynolds J, Krapels K, Fanning J, Corbin T. Review of Bayer pattern color filter array (CFA) demosaicing with new quality assessment algorithms. Army Research Lab Adelphi Md Sensors and Electron Devices Directorate. 2010;1–29. https://doi.org/10.21236/ada513752

57. Radke RJ, Andra S, Al-Kofahi O, Roysam B. Image change detection algorithms: a systematic survey. IEEE Trans Image Process. 2005; 14(3):294–307. https://doi.org/10.1109/tip.2004.838698 PMID: 15762326

58. Urbanek S. jpeg: Read and write JPEG images. 2019. Available from: https://CRAN.R-project.org/package=jpeg.

59. Brockwell PJ, Davis RA. Introduction to time series and forecasting. Springer International Publishing, Switzerland; 2016. pp.1–39. https://doi.org/10.1007/978-3-319-29854-2

60. Robertson MB, Köhler U, Hoskins PR, Marshall I. Quantitative analysis of PC MRI velocity maps: pulsatile flow in cylindrical vessels. Magn Reson Imaging. 2001; 19(5):685–695. https://doi.org/10.1016/s0730-725x(01)00376-9 PMID: 11672627

61. Kongnuan S, Pholuang J. A Fourier series-based analytical solution for the oscillating airflow in a human respiratory tract. Int J Pure Appl Math. 2012; 78(5):721–733. Available from: https://ijpam.eu/contents/2012-78-5/11/11.pdf.

62. Whitlock MC, Schluter D. Data transformations. In: The analysis of biological data. Roberts and Company Publishers, CO, United States; 2009. pp.326–332.

63. Pinheiro JC, Bates DM. Linear mixed-effects models: basic concepts and examples. In: Mixed-Effects Models in S and S-PLUS. Springer; 2000. p. 3–56. https://doi.org/10.1007/b98882

64. Bolker BM, Brooks ME, Clark CJ, Geange SW, Poulsen JR, Stevens MHH, et al. Generalized linear mixed models: a practical guide for ecology and evolution. Trends Ecol Evol. 2009; 24(3):127–135. https://doi.org/10.1016/j.tree.2008.10.008 PMID: 19185386

65. Nakagawa S, Schielzeth H. A general and simple method for obtaining R^2 from generalized linear mixed-effects models. Methods Ecol Evol. 2013; 4(2):133–142. https://doi.org/10.1111/j.2041-210x.2012.00261.x

66. Portney LG, Watkins MP. Multivariate analysis. In: Foundations of clinical research: applications to practice. Vol 892. Pearson/Prentice Hall, Upper Saddle River, NJ, United States; 2009. pp. 587–620.

67. Li JK. Hemodynamics of large arteries. In: Dynamics of the vascular system. Vol 1. World Scientific Publishing Co Pte Ltd, Singapore; 2004. pp. 76–141. https://doi.org/10.1142/9789812562661_0003

68. Fung YC. Blood Flow in Arteries. In: Biomechanics: circulation. 2nd ed. Springer-Verlag, New York, United States; 2013. pp. 108–205. https://doi.org/10.1007/978-1-4757-2696-1

69. Fung YC. The Veins. In: Biomechanics: circulation. 2nd ed. Springer-Verlag, New York; 2013. pp. 206–265. https://doi.org/10.1007/978-1-4757-2696-1

70. Li JK, Melbin J, Riffle RA, Noordergraaf A. Pulse wave propagation. Circ Res. 1981; 49(2):442–452. https://doi.org/10.1161/01.res.49.2.442 PMID: 7249280

71. Womersley J. Oscillatory flow in arteries: the constrained elastic tube as a model of arterial flow and pulse transmission. Phys Med Biol. 1957; 2(2):178–187. https://doi.org/10.1088/0031-9155/2/2/305 PMID: 13484470

72. Bertram C. Energy dissipation and pulse wave attenuation in the canine carotid artery. J Biomech. 1980; 13(12):1061–1073. https://doi.org/10.1016/0021-9290(80)90050-0 PMID: 7204422

73. McDonald D, Gessner U. Wave attenuation in viscoelastic arteries. In: International Conference on Hemorheology. Edited by A.L. Copley. Pergamon Press Oxford, New York, United States; 1968. p. 113–125.

74. Bergel D. The static elastic properties of the arterial wall. J Physiol. 1961; 156(3):448–469. https://doi.org/10.1113/jphysiol.1961.sp006687

75. Nichols W, O'Rourke M, Vlachopoulos C. McDonald's blood flow in arteries: theoretical, experimental and clinical principles. CRC press, Taylor & Francis Group, Florida, United States; 2011.

76. Bergel D. The dynamic elastic properties of the arterial wall. J Physiol. 1961; 156(3):445–457. https://doi.org/10.1113/jphysiol.1961.sp006686 PMID: 16992075

77. Anliker M, Histand MB, Ogden E. Dispersion and attenuation of small artificial pressure waves in the canine aorta. Circ Res. 1968; 23(4):539–551. https://doi.org/10.1161/01.res.23.4.539 PMID: 5677945

78. McDonald D. The flow properties of blood as a factor in the stability of pulsatile flow: Proceedings of The 4th International Congress on Rheology; 1965; New York Medical College. New York, United States. Interscience Publishers Inc. p. 205–213.

79. McDonald D. Regional pulse-wave velocity in the arterial tree. J Appl Physiol. 1968; 24(1):73–78. https://doi.org/10.1152/jappl.1968.24.1.73 PMID: 5635773

80. Li JK, Melbin J, Campbell K, Noordergraaf A. Evaluation of a three point pressure method for the determination of arterial transmission characteristics. J Biomech. 1980; 13(12):1023–1029. https://doi.org/10.1016/0021-9290(80)90046-9 PMID: 7204418

81. Milnor W, Bertram C. The relation between arterial viscoelasticity and wave propagation in the canine femoral artery in vivo. Circ Res. 1979; 43(1):870–879. https://doi.org/10.1161/01.res.43.6.870

82. Feher JJ. Vascular function: Hemodynamics. In: Quantitative Human Physiology: An introduction. Elsevier-Academic Press, Cambridge, MA, United States; 2012. pp. 498–507. https://doi.org/10.1016/C2009-0-64018-6

83. Nichols WW, Edwards DG. Arterial elastance and wave reflection augmentation of systolic blood pressure: deleterious effects and implications for therapy. J Cardiovasc Pharmacol Ther. 2001; 6(1):5–21. https://doi.org/10.1177/107424840100600102 PMID: 11452332

84. Moreno AH, Katz AI, Gold LD, Reddy R. Mechanics of distension of dog veins and other very thin-walled tubular structures. Circ Res. 1970; 27(6):1069–1080. https://doi.org/10.1161/01.res.27.6.1069 PMID: 5494860

85. Keener J, Sneyd J. The circulatory system. In: Mathematical Physiology II: Systems Physiology. Springer-Verlag, New York; 2009. pp. 471–522. https://doi.org/10.1007/978-0-387-79388-7

86. Burton AC. Arrangements of Many Vessels. In: Physiology and biophysics of the circulation: an introductory text. 2nd ed. Year Book Medical Publishers, Chicago, United States; 1972. pp.51–62.

87. Caro CG, Pedley TJ, Schroter RC, Seed WA, Parker KH. The systemic veins. In: The mechanics of the circulation. 2nd ed. Cambridge University Press, Cambridge, United States; 2012. pp. 426–466. https://doi.org/10.1017/CBO9781139013406

88. Hogan MJ, Feeney L. The ultrastructure of the retinal blood vessels: I. The large vessels. J Ultrastruct Res. 1963; 9(1-2):10–28. https://doi.org/10.1016/S0022-5320(63)80035-0

89. Morgan WH, Yu DY, Alder VA, Cringle SJ, Constable IJ. Relation between pressure determined by ophthalmodynamometry and aortic pressure in the dog. Br J Ophthalmol. 1998; 82(7):821–825. https://doi.org/10.1136/bjo.82.7.821 PMID: 9924380

90. Lam J, Chan G, Morgan WH, Hazelton M, Betz-Stablein B, Cringle SJ, et al. Structural characteristics of the optic nerve head influencing human retinal venous pulsations. Exp Eye Res. 2016; 145:341–346. https://doi.org/10.1016/j.exer.2016.02.003 PMID: 26892807

91. Guidoboni G, Harris A, Cassani S, Arciero J, Siesky B, Amireskandari A, et al. Intraocular pressure, blood pressure, and retinal blood flow autoregulation: A mathematical model to clarify their relationship and clinical relevance. Invest Ophthalmol Visual Sci. 2014; 55(7):4105–4118. https://doi.org/10.1167/iovs.13-13611

92. Harris A, Joos K, Kay M, Evans D, Shetty R, Sponsel WE, et al. Acute IOP elevation with scleral suction: effects on retrobulbar haemodynamics. Br J Ophthalmol. 1996; 80(12):1055–1059. https://doi.org/10.1136/bjo.80.12.1055 PMID: 9059269

93. Findl O, Strenn K, Wolzt M, Menapace R, Vass C, Eichler HG, et al. Effects of changes in intraocular pressure on human ocular haemodynamics. Curr Eye Res. 1997; 16(10):1024–1029. https://doi.org/10.1076/ceyr.16.10.1024.9024 PMID: 9330854

94. Conway ML, Wevill M, Benavente-Perez A, Hosking SL. Ocular blood-flow hemodynamics before and after application of a laser in situ keratomileusis ring. J Cataract Refr Surg. 2010; 36(2):268–272. https://doi.org/10.1016/j.jcrs.2009.09.013

95. Levine DN. Spontaneous pulsation of the retinal veins. Microvasc Res. 1998; 56(3):154–165. https://doi.org/10.1006/mvre.1998.2098 PMID: 9828153

96. Conrad WA. Pressure-flow relationships in collapsible tubes. IEEE Trans Biomed Eng. 1969; 16(4):284–295. https://doi.org/10.1109/tbme.1969.4502660 PMID: 5354907

97. Heil M. Stokes flow in collapsible tubes: computation and experiment. J Fluid Mech. 1997; 353:285–312. https://doi.org/10.1017/S0022112097007490

98. Portnoy HD, Chopp M. Cerebrospinal fluid pulse wave form analysis during hypercapnia and hypoxia. Neurosurgery. 1981; 9(1):14–27. https://doi.org/10.1227/00006123-198107000-00004 PMID: 7279168

99. Cheung N, Islam FA, Jacobs DR, Jr, Sharrett AR, Klein R, Polak JF, et al. Arterial compliance and retinal vascular caliber in cerebrovascular disease. Ann Neurol. 2007; 62(6):618–624. https://doi.org/10.1002/ana.21236 PMID: 17918248

100. Kawasaki R, Cheung N, Wang JJ, Klein R, Klein BE, Cotch MF, et al. Retinal vessel diameters and risk of hypertension: the Multiethnic Study of Atherosclerosis. J Hypertens. 2009; 27(12):2386. https://doi.org/10.1097/HJH.0b013e3283310f7e PMID: 19680136

101. Winer N, Sowers JR. Vascular compliance in diabetes. Curr Diab Rep. 2003; 3(3):230–234. https://doi.org/10.1007/s11892-003-0069-y PMID: 12762971

102. Lim LS, Chee ML, Cheung CY, Wong TY. Retinal vessel geometry and the incidence and progression of diabetic retinopathy. Invest Ophthalmol Visual Sci. 2017; 58(6):200–205. https://doi.org/10.1167/iovs.17-21699

103. Hamer J, Alberti E, Hoyer S, Wiedemann K. Influence of systemic and cerebral vascular factors on the cerebrospinal fluid pulse waves. J Neurosurg. 1977; 46(1):36–45. https://doi.org/10.3171/jns.1977.46.1.0036 PMID: 830813

104. Bateman GA. Vascular compliance in normal pressure hydrocephalus. Am J Neuroradiol. 2000; 21(9):1574–1585. PMID: 11039334